The Astrophysical Journal Supplement Series, 174:426–454, 2008 February

PLANETARY NEBULAE DETECTED IN THE *SPITZER SPACE TELESCOPE* GLIMPSE LEGACY SURVEY

Sun Kwok and Yong Zhang
Department of Physics, University of Hong Kong, Hong Kong; sunkwok@hku.hk

Nico Koning
University of Calgary, Calgary, AB T2N 1N4, Canada

Hsiu-Hui Huang
Institute of Astronomy and Astrophysics, Academia Sinica, Taipei, Taiwan

and

E. Churchwell
Department of Astronomy, University of Wisconsin-Madison, Madison, WI 53706
Received 2007 June 30; accepted 2007 August 15

ABSTRACT

We detected and imaged 30 planetary nebulae in the *Sptizer Space Telescope* Galactic Legacy Infrared Mid-Plane Survey Extraordinaire (GLIMPSE) survey. The distribution of warm dust is clearly shown in these images. From the derived fluxes at the 3.6, 4.5, 5.8, and 8.0 μm bands we are able to separate the photospheric, nebular, and dust emission components in the nebulae.

Subject headings: planetary nebulae: general — stars: AGB and post-AGB

1. INTRODUCTION

Planetary nebulae (PNs) are traditionally characterized by their optical emission-line spectrum arising from their ionized gas component. Multiwavelength observations of PNs, however, show that PNs undergo a rich variety of radiation mechanisms, including millimeter/submillimeter line radiation from the molecular component, X-ray continuum from the shocked bubble, radio free-free continuum emission from the ionized component, and infrared emission from the dust component (Kwok 2000). From results of the *IRAS* survey, we learned the dust component has typical color temperatures of 100–200 K, and dust emission accounts for as much as $\sim$1/3 of the total energy output of the nebulae (Zhang & Kwok 1991). At wavelengths $\lambda > 5$ μm, the dust component is expected to dominate over bound-free emission from the ionized component. Because the 5–8 μm spectral region is difficult to observe from the ground, the spectral energy distribution of PNs in this region is not well known. The *Spitzer Space Telescope* (*Spitzer*) is capable of performing imaging with high spatial resolution and sensitivity in the 3–8 μm region and offers the possibility of mapping the dust distribution of PNs. In this paper, we report our search and observations of PN candidates in the area covered by the Galactic Legacy Infrared Mid-Plane Survey Extraordinaire (GLIMPSE) survey, one of the Legacy Science Projects of *Spitzer*. Through the experience learned from this exercise, we hope to be able to better characterize the spectral behavior of PNs in the transition spectral region between the nebular and dust components and to distinguish between PNs, compact H II regions, and other stellar objects.

2. OBSERVATION

The data reported here were taken as part of the GLIMPSE survey. Observations were obtained over the periods between 2004 March 9 and 2004 November 1 with the Infrared Array Camera (IRAC; Fazio et al. 2004) on *Spitzer*. IRAC has four wavelength bands centered at 3.6, 4.5, 5.8, and 8.0 μm, each of which has a field of view (FOV) of $\sim 5.2' \times 5.2'$. The detectors for the 3.6 and 4.5 μm bands are 256×256 pixel InSb arrays operating at $\sim$15 K. The detectors for the 5.8 and 8.0 μm bands are 256×256 pixel Si: As arrays operating at $\sim$6 K. All four bands are observed simultaneously. The 3.6 and 5.8 μm bands FOVs are coincident on the sky and the 4.5 and 8.0 μm bands FOVs are coincident, but the center positions of the two pairs are offset by 6.73′. The pixel size in all four bands is $\sim 1.22''$. The FWHM of the point-spread functions was $1.63''$, $1.70''$, $1.85''$, and $1.94''$ at the 3.6, 4.5, 5.8, and 8.0 μm bands, respectively.

The GLIMPSE survey covers the inner two-thirds of the Galactic plane ($l = \pm 10^\circ - 65^\circ$, $b = \pm 1^\circ$; total area $\sim$220 deg^2) in all four IRAC bands. Details of the survey is described in Churchwell et al. (2004).

3. DATA PROCESSING

Data processing is performed by both the *Spitzer* Science Center (SSC) and by the GLIMPSE team at the University of Wisconsin–Madison. The SSC archive provides these types of data to the public:

1. Raw data that have undergone no processing other than being populated with auxiliary science telemetry keywords. These data are provided in the rare case that an observer wishes to process the data in a manner different than that of the SSC.
2. Basic calibrated data (BCD) is exposure level data that have been through the IRAC pipeline. These data have gone through such processing as the removal of instrumental signatures, calibration into physical units and the addition of pointing information. One BCD is provided for each integration taken by IRAC as well as several complimentary files. These files generally contain information about the quality of each pixel; provided so one can assess the quality of and, if needed, repair each image.

A more detailed explanation of the SSC data processing can be found in the *Spitzer* Observer's Manual, § 6.3.[1]

After the BCD, the GLIMPSE team combined the images into $2^\circ \times 2^\circ$ mosaics and took extra steps to correct for further instrumental artifacts such as the correction of zodiacal background,

[1] See http://ssc.spitzer.caltech.edu/documents/som/.

excessive cosmic-ray hits, and other instrumental and downlink problems. Next, the flux densities and positions of point sources are determined using DAOPHOT, and the position of brighter sources are checked against the 2MASS Point Source Catalogue. The point-source extraction is an iterative process where the extracted sources are removed, then the residual image (image-point sources) is plotted to check if a smooth background is observed or if there is a dip or bright spot where a source was extracted. A second iteration was made to compensate for either a dip (too much flux was extracted) or a bright spot (too little flux extracted). This type of iteration was continued until the place where a source was extracted was no longer identifiable. Particular care is invested in accurately extracting point source fluxes when a source is located in a bright and spatially variable background such as occurs around the central stars of PNs. Of course, as the background becomes brighter and has strong gradients, photometric accuracy does suffer and the corresponding errors are larger.

The point-source lists obtained in the eight pointed observations (2×2 s frames in each of the four bands) are merged to produce input for the generation of the GLIMPSE Point Source Catalog and GLIMPSE Point Source Archive. The data are resampled, registered to a Galactic coordinate system, and IRAC frames are background matched, if necessary. The resulting images are turned into tiles of mosaicked images of 200×200 pixels with pixel sizes of approximately $0.6''$.

The processed data sets are compared with the Macquarie/AAO/Strasbourg Catalogue of Galactic Planetary Nebulae (MASH; Parker et al. 2003a, 2006). This catalog is a combination of the Strasbourg-ESO Catalogue of Galactic Planetary Nebulae (Acker et al. 1992, 1996) and new PNs identified in the high-resolution AAO/UKSAT Hα survey of the Milky Way (Parker et al. 1999, 2003b). For each PN that lies in the GLIMPSE field, the corresponding GLIMPSE images are loaded into DS9 in a tiled pattern so each of the four bands can be seen at once. The images are then centered on the coordinates of the PN. After zooming to an appropriate level, the four-band images are extracted.

The GLIMPSE Point Source Catalogue contains about 30 million sources, with a listing of the designation, position, and flux of each, along with errors. A larger ($\sim 5 \times 10^7$) point source archive compiled with less stringent reliability requirements is also produced.

To obtain the total fluxes of extended sources, we first draw a box around the nebulae. The fluxes of all pixels within the box are totaled and converted to units of mJy. The sum of all the fluxes of sources found in the point-source archive within the box is then subtracted off this total to derive a net flux. A box of the same size is also made on an "off" position away from the nebula. The net flux in this "off" position is then calculated using the same procedure as the "on" position. Subtraction of the "off" net flux from the "on" net flux gives the total flux of the nebula.

4. RESULTS

A total of 30 PNs were detected. The four-band IRAC images of these PNs are displayed in Figures 1–15. The measured total fluxes in the four IRAC bands are listed in Table 1.

4.1. *Spectral Energy Distribution*

Additional fluxes were extracted from other data archives: the Two Micron All Sky Survey (2MASS), Deep Near Infrared Survey of the Southern Sky (DENIS), *Midcourse Space Experiment* (*MSX*), and the *Infrared Astronomical Satellite* Point Source Catalogue (*IRAS* PSC). The magnitude and fluxes of these measurements are tabulated in Table 2. By combining all the data, we are able to construct spectral energy distributions (SEDs) of the detected sources, and each individual SED is displayed in Figure 16. For some of the PNs with a large size, the data given by these point source database only represent the lower limit of fluxes. These objects are not included in Table 2 and Figure 16, even though they may be detected by these surveys. In some cases (e.g., PNG 302.3−00.5, PNG 321.0−00.6, PNG 333.9+00.6), the *JHK* measurement arise from the central star, and the stellar continuum is clearly separated from the nebular emission seen in the IRAC bands. As the stellar continuum is sharply decreasing with increasing wavelength, their contributions to the IRAC fluxes are probably negligible. We should note therefore that the *JHK* points presented in Figure 16 represent mostly the central star fluxes, but not necessarily the total fluxes from the nebulae. They are plotted mainly to illustrate the relative contributions of the central star and the nebula in different spectral regions.

4.2. *IRAC Colors*

Using the IRAC four-band photometry, we have constructed color-color diagrams for the detected PNs from the $[3.6]-[4.5]$ and $[5.8]-[8.0]$ colors, and the results are plotted in Figure 17. For starlike objects (blackbodies), their location on the plot will be at the (0, 0) point. This is the case for PNG 342.7+00.7, which has a blackbody spectrum of about 1500 K (Fig. 16). The IRAC colors of PNG 306.4+00.2 are unlike those of a dust spectrum but instead resemble the Rayleigh-Jeans tail of a blackbody of $\sim$1000 K.

The colors of our sample objects are generally very red and cluster around colors of $[3.6]-[4.5] \sim 1$ and $[5.8]-[8.0] \sim 2$. There are two objects (PNG 333.9+00.6, PNG 322.4−00.1) that have redder colors and do not belong to this cluster. The peculiar color of PNG 333.9+00.6 is due to the faintness of the 3.6 μm point, otherwise the IRAC colors should follow nicely a reddened photospheric spectrum (Fig. 16). For PNG 322.4−00.1, the IRAC photometry agrees well with the *ISO* spectrum of the object. The peculiar color of PNG 322.4−00.1 can be attributed to the sharply rising spectrum between 6 and 10 μm.

For comparison, Figure 17 also gives the colors presented by Hora et al. (2004) for six PNs, and the model predictions for young and evolved PNs (Cohen et al. 2007). These points are located at approximately the same position in the color-color diagram of our sample, although the models seem to slightly overestimate the $[3.6]-[4.5]$ colors.

4.3. *Individual Objects*

4.3.1. *PNG 010.1+00.7*

PNG 010.1+00.7 [=NGC 6537 = IRAS 18021−1950; R.A.(J2000.0) $= 18^{\rm h}05^{\rm m}13.3^{\rm s}$, decl.(J2000.0) $= -19^\circ 50' 13.6''$] is a type I PN with bipolar structure and has a central star with a temperature in the range $(1.5–2.5) \times 10^5$ K (Matsuura et al. 2005). Pottasch et al. (2000) obtained a nitrogen to oxygen ratio of 2.4 for the PN. It was detected in the DENIS, 2MASS, *MSX*, and *IRAS* surveys, as well as by *Spitzer* in all four IRAC bands (Fig. 1). The *IJK* photometry of the PN with DENIS has been presented by Schmeja & Kimeswenger (2002). The PN was also detected by the NRAO VLA Sky Survey (NVSS; Condon & Kaplan 1998), which measured a flux density of 428 ± 13 mJy at 1.4 GHz. NGC 6537 was observed with the *ISO* Short Wavelength Spectrometer (SWS) and Long Wavelength Spectrometer (LWS), covering

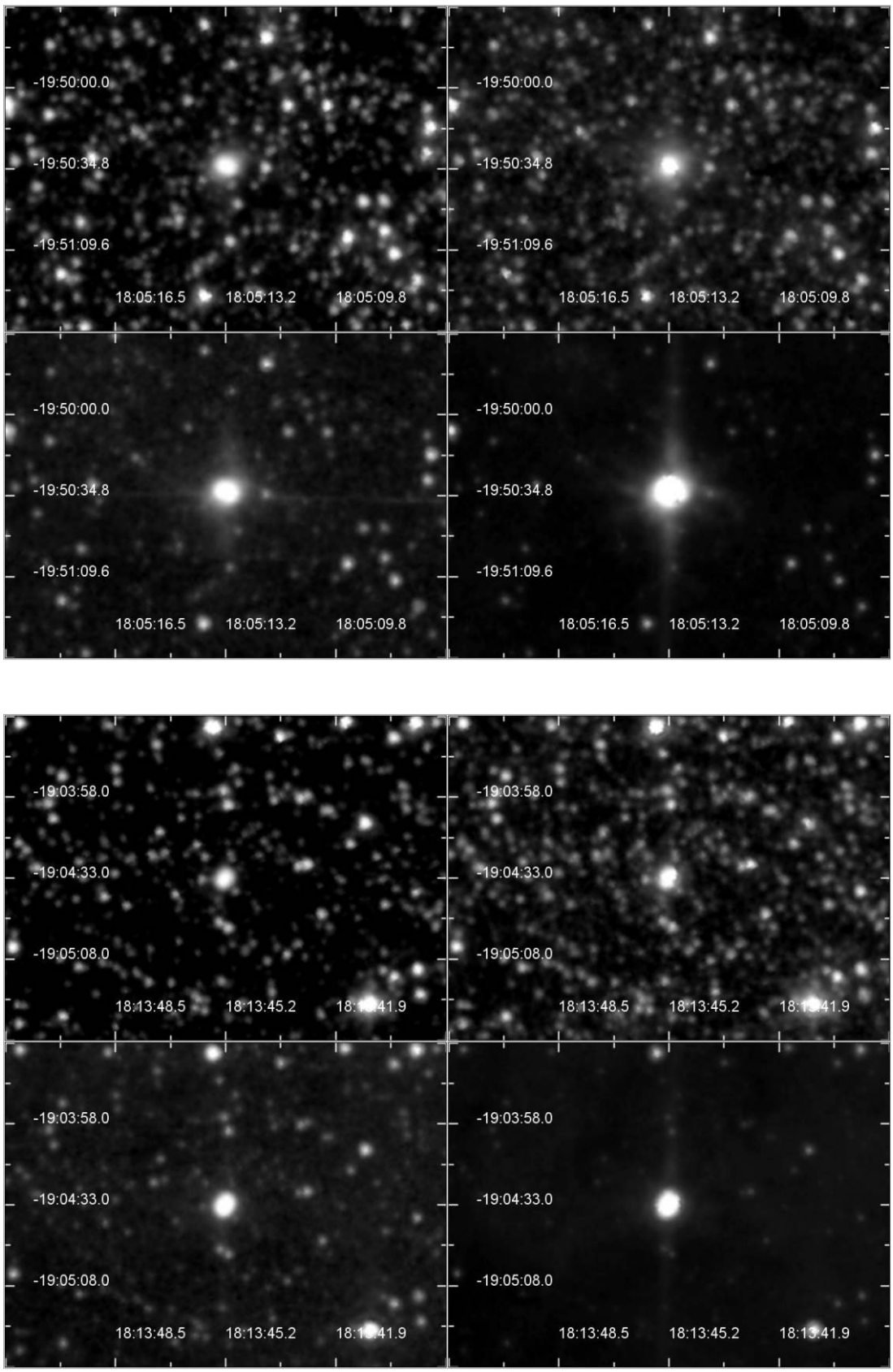

FIG. 1.—SSC IRAC images of NGC 6537 (*top*) and NGC 6567 (*bottom*). The images for each object are arranged as follows: *top left*: 3.6 μm; *top right*: 4.5 μm; *bottom left*: 5.8 μm; *bottom right*: 8.0 μm. The coordinates are in units of R.A. (J2000.0 on the horizontal scale) and decl. (J2000.0 on the vertical scale).

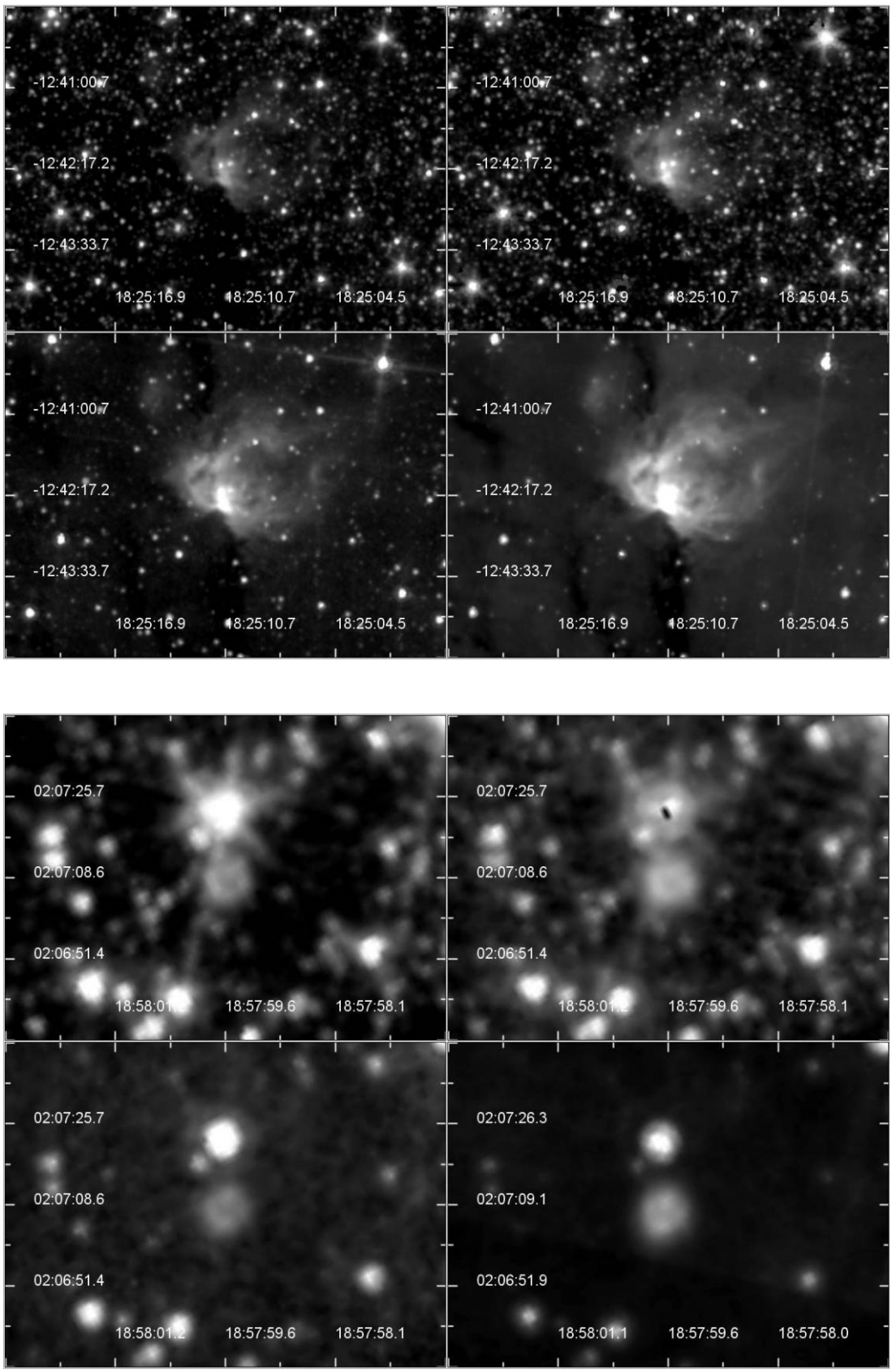

FIG. 2.—SSC IRAC images of PNG 018.6−00.0 (*top*) and PNG 035.5−00.4 (*bottom*). The order of images are arranged as Fig. 1.

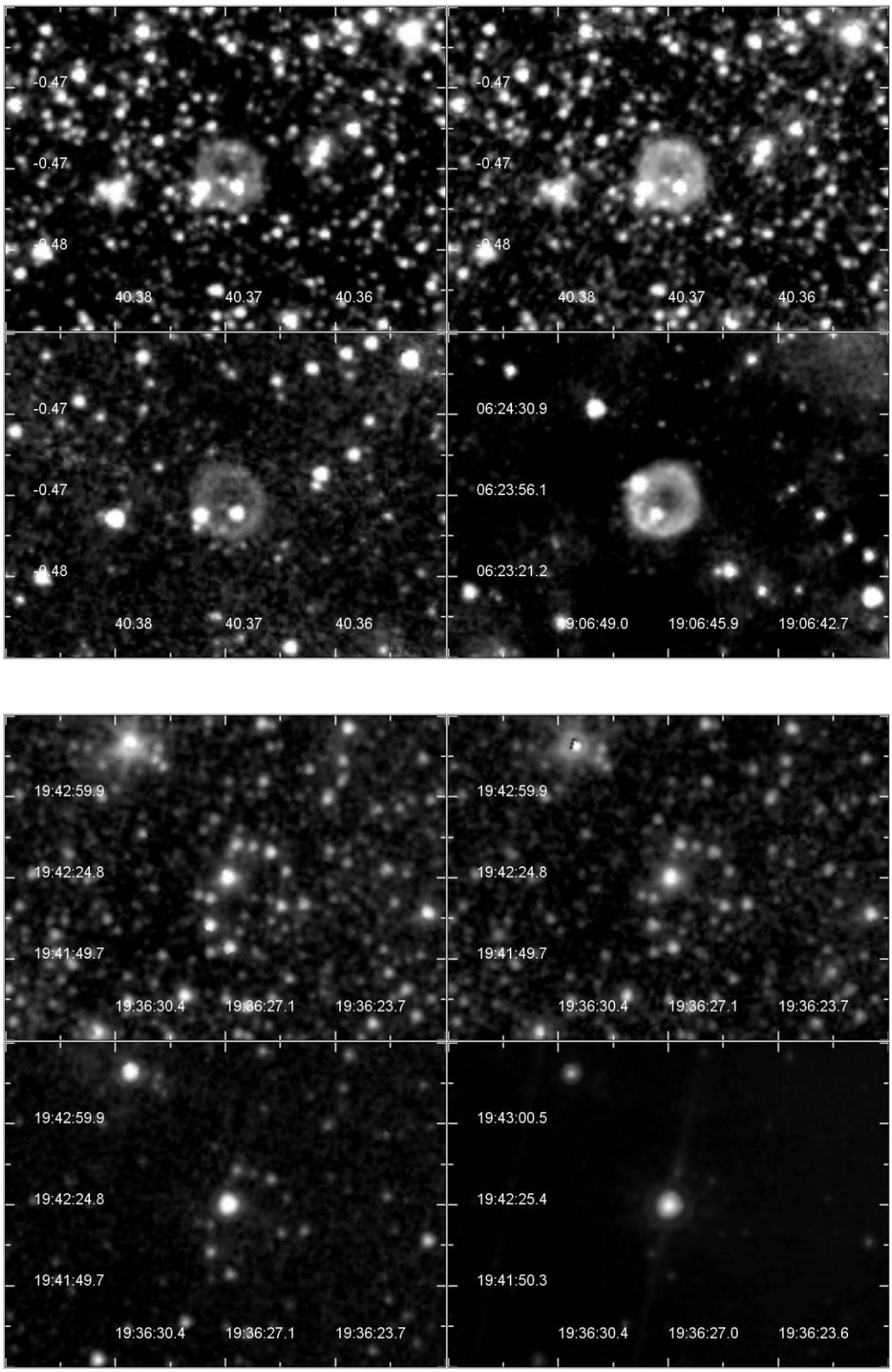

FIG. 3.— SSC IRAC images of A53 (*top*) and M1-71 (*bottom*). The order of images are arranged as Fig. 1.

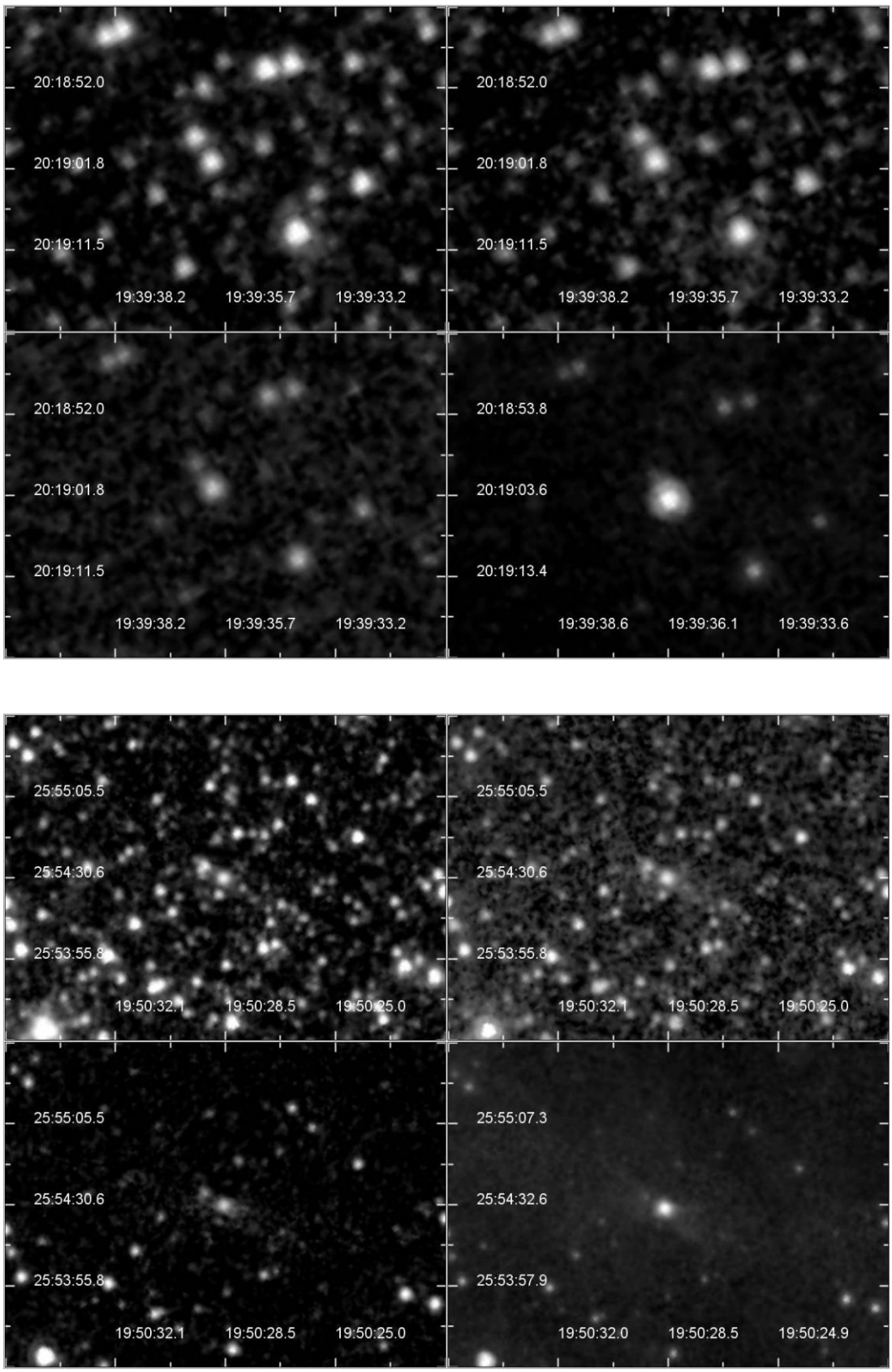

FIG. 4.—SSC IRAC images of K3-42 (*top*) and M2-48 (*bottom*). The order of images are arranged as Fig. 1.

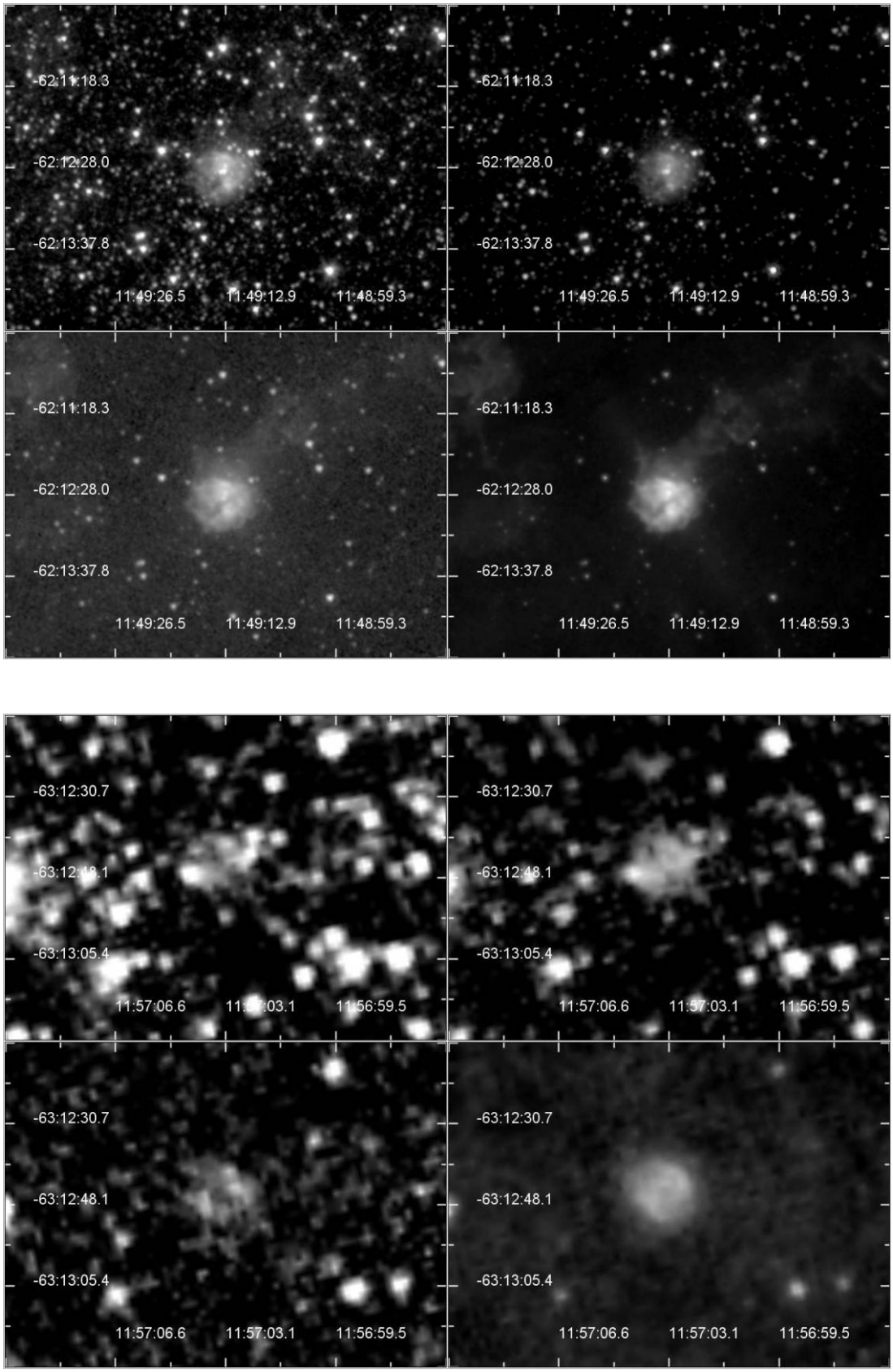

FIG. 5.—SSC IRAC images of PNG 295.7−00.2 (*top*) and PNG 296.8−00.9 (*bottom*). The order of images are arranged as Fig. 1.

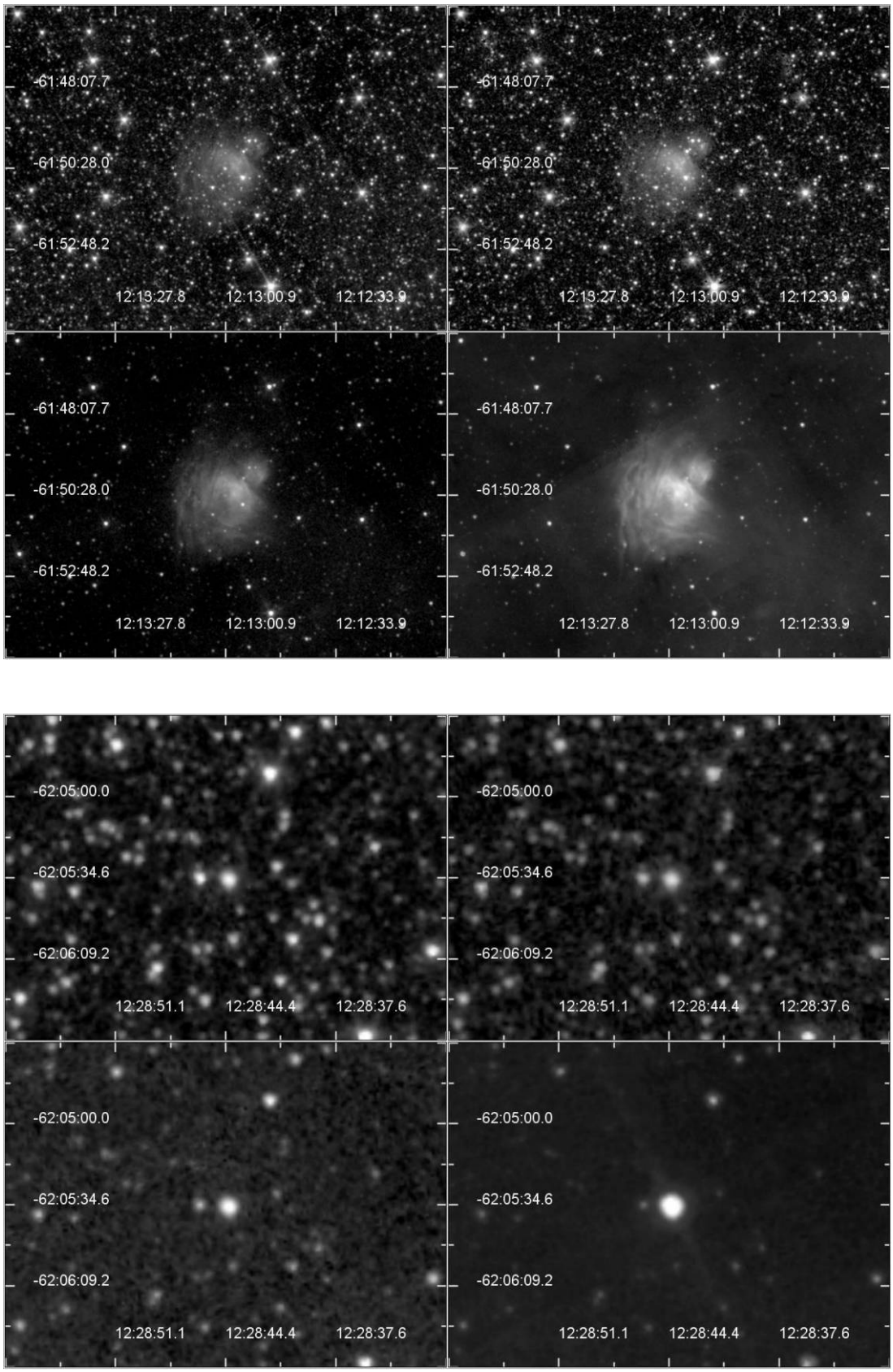

FIG. 6.—SSC IRAC images of PNG 298.4+00.6 (*top*) and He 2-83 (*bottom*). The order of images are arranged as Fig. 1.

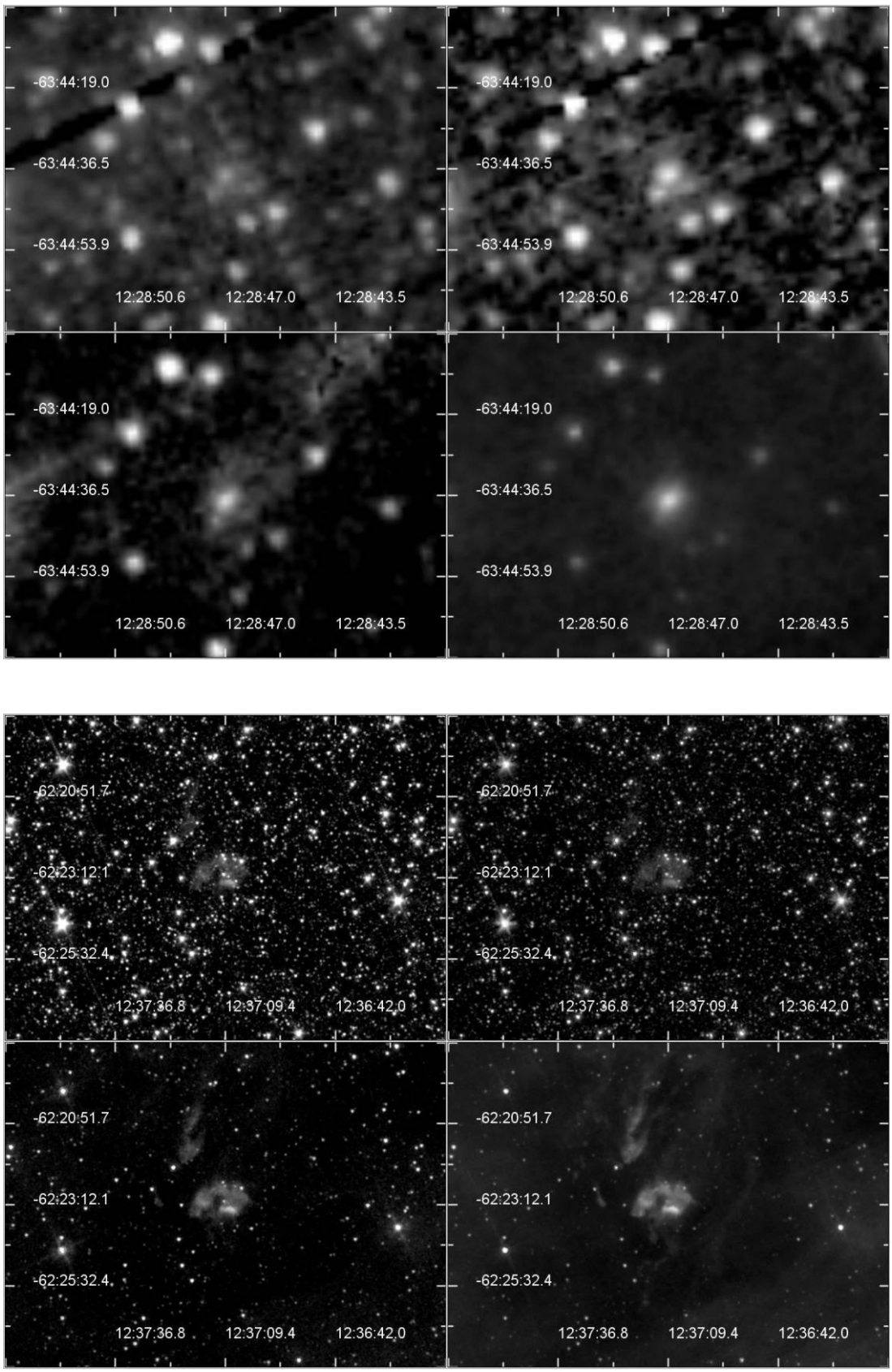

FIG. 7.—SSC IRAC images of PNG He 2-84 (top) and PNG 301.1+00.4 (*bottom*). The order of images are arranged as Fig. 1.

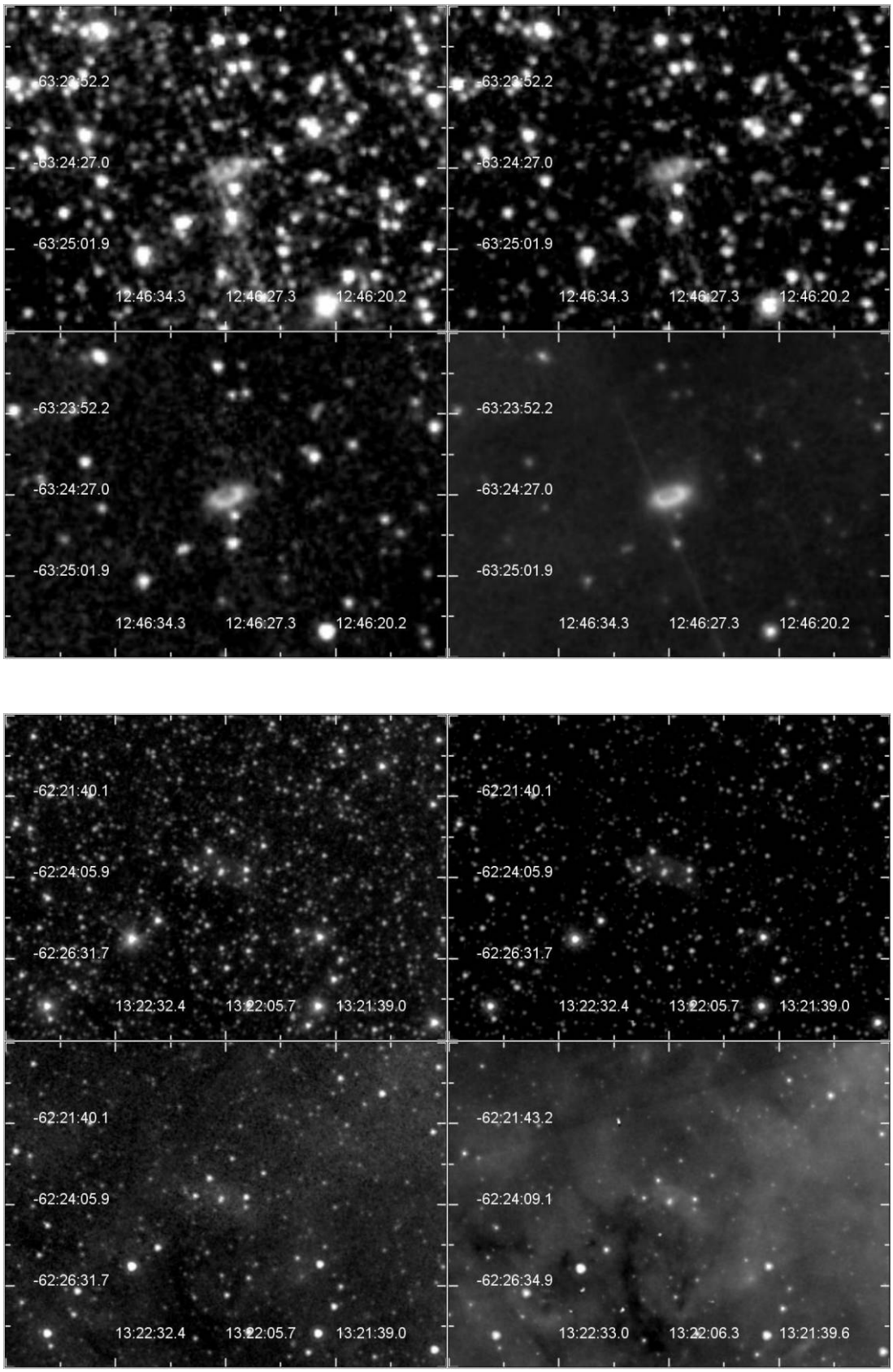

FIG. 8.—SSC IRAC images of PNG 302.3+00.5 (top) and PNG 306.4+00.2(*bottom*). The order of images are arranged as Fig. 1.

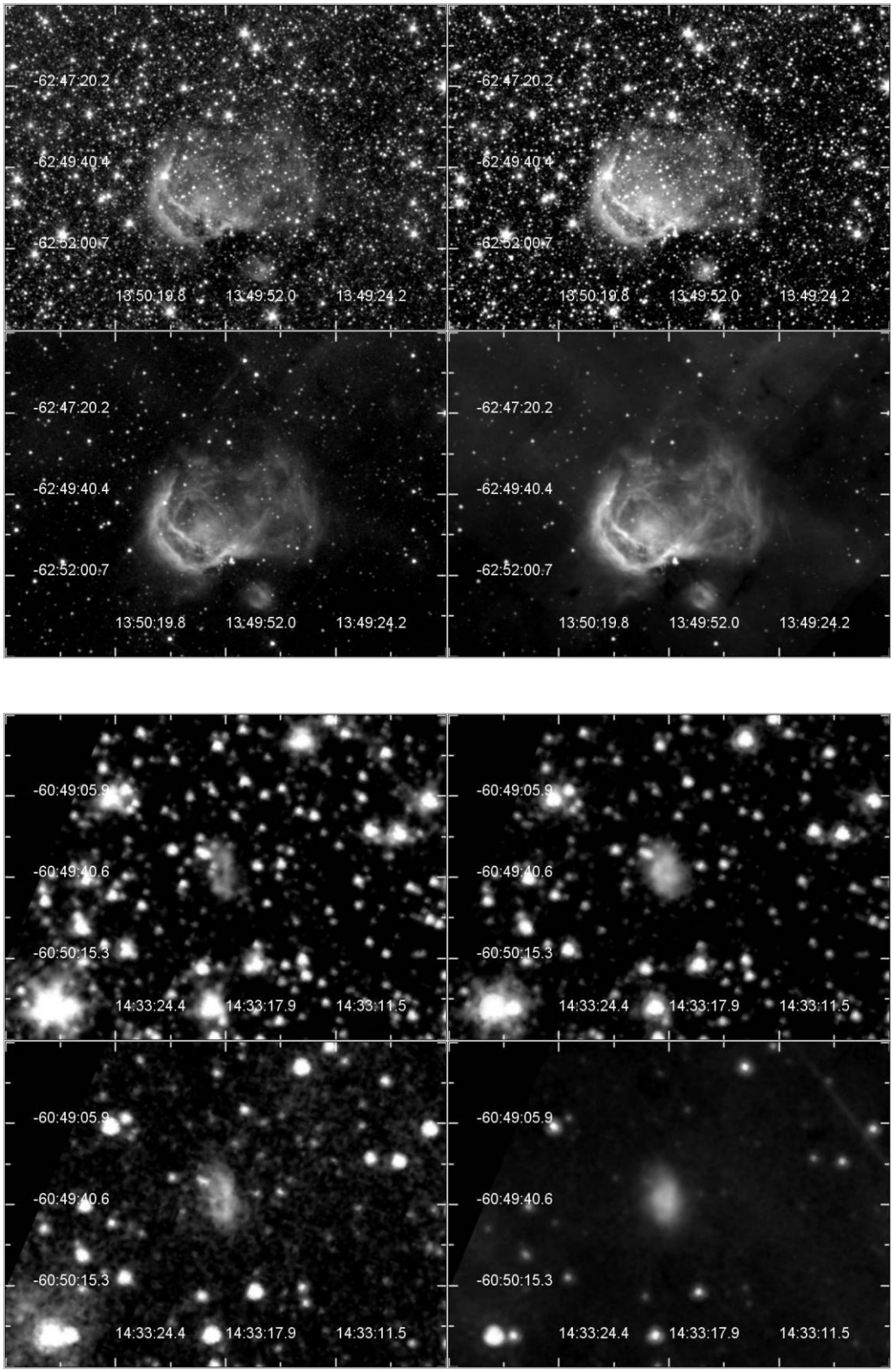

FIG. 9.—SSC IRAC images of PNG 309.5−00.7 (*top*) and He 2-111 (*bottom*). The order of images are arranged as Fig. 1.

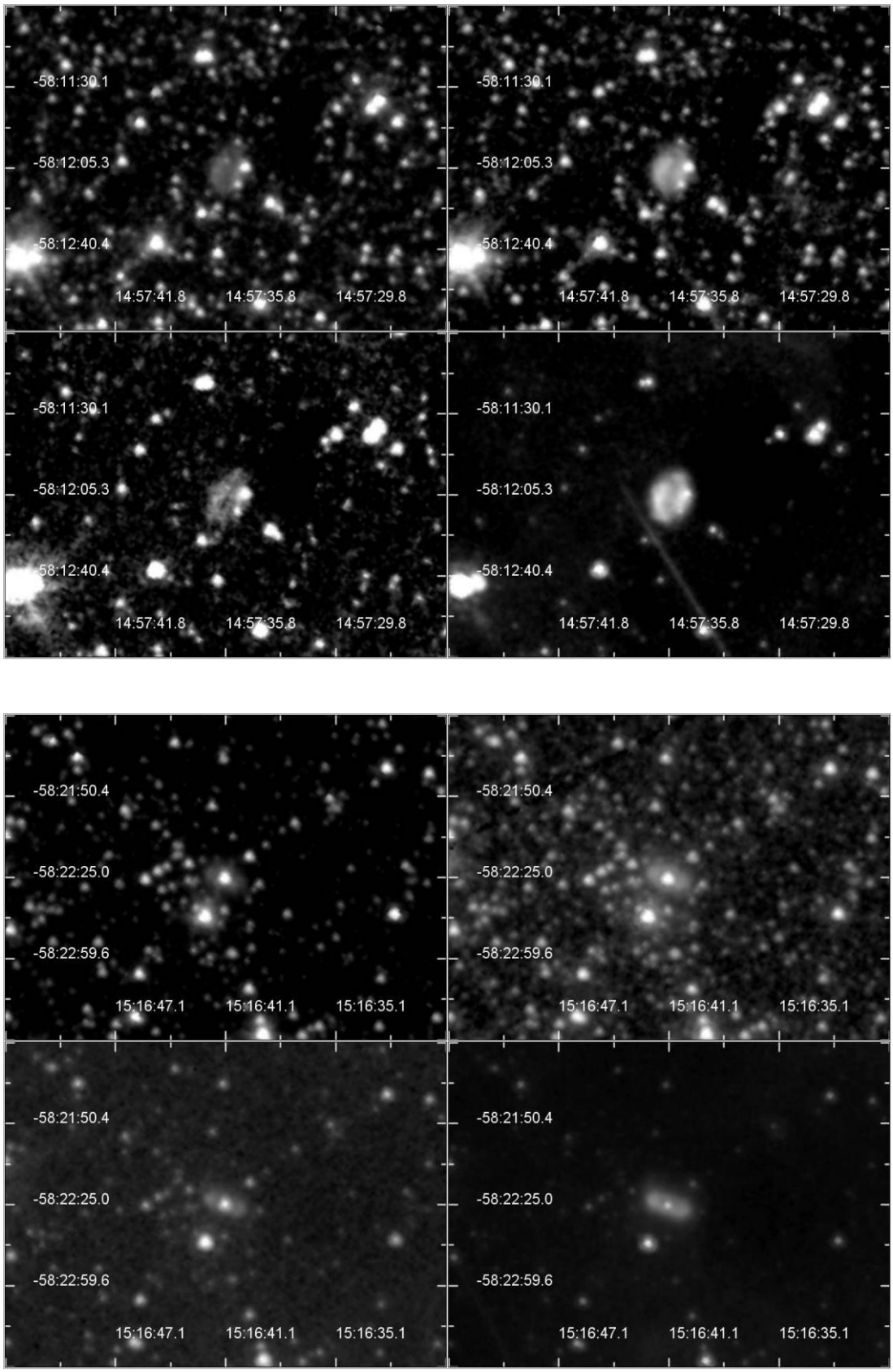

FIG. 10.—SSC IRAC images of PNG 318.9+00.6 (*top*) and PNG 321.0−00.7 (*bottom*). The order of images are arranged as Fig. 1.

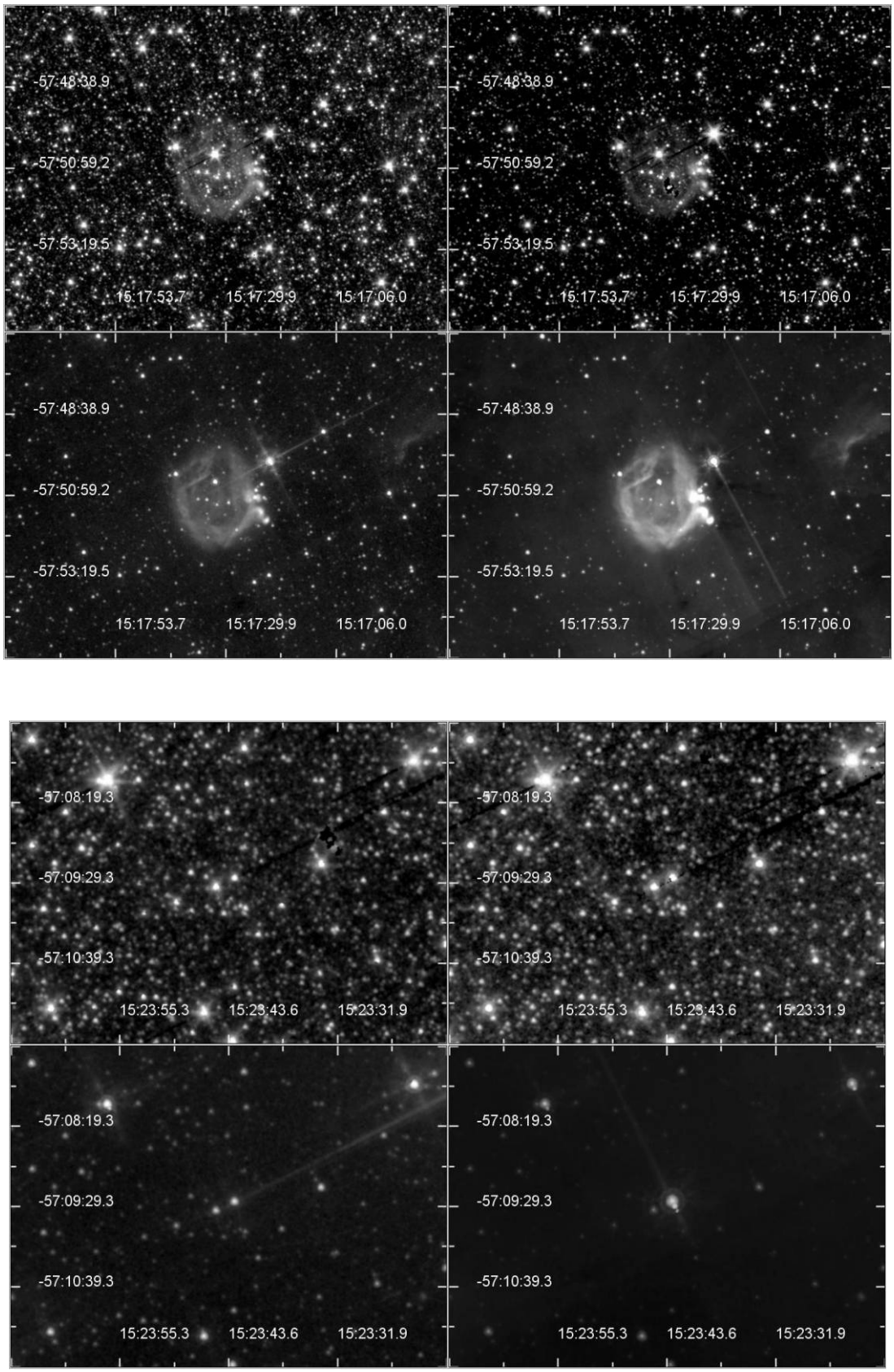

FIG. 11.—SSC IRAC images of PNG 321.3−00.3 (*top*) and PNG 322.4−00.1 (*bottom*). The order of images are arranged as Fig. 1.

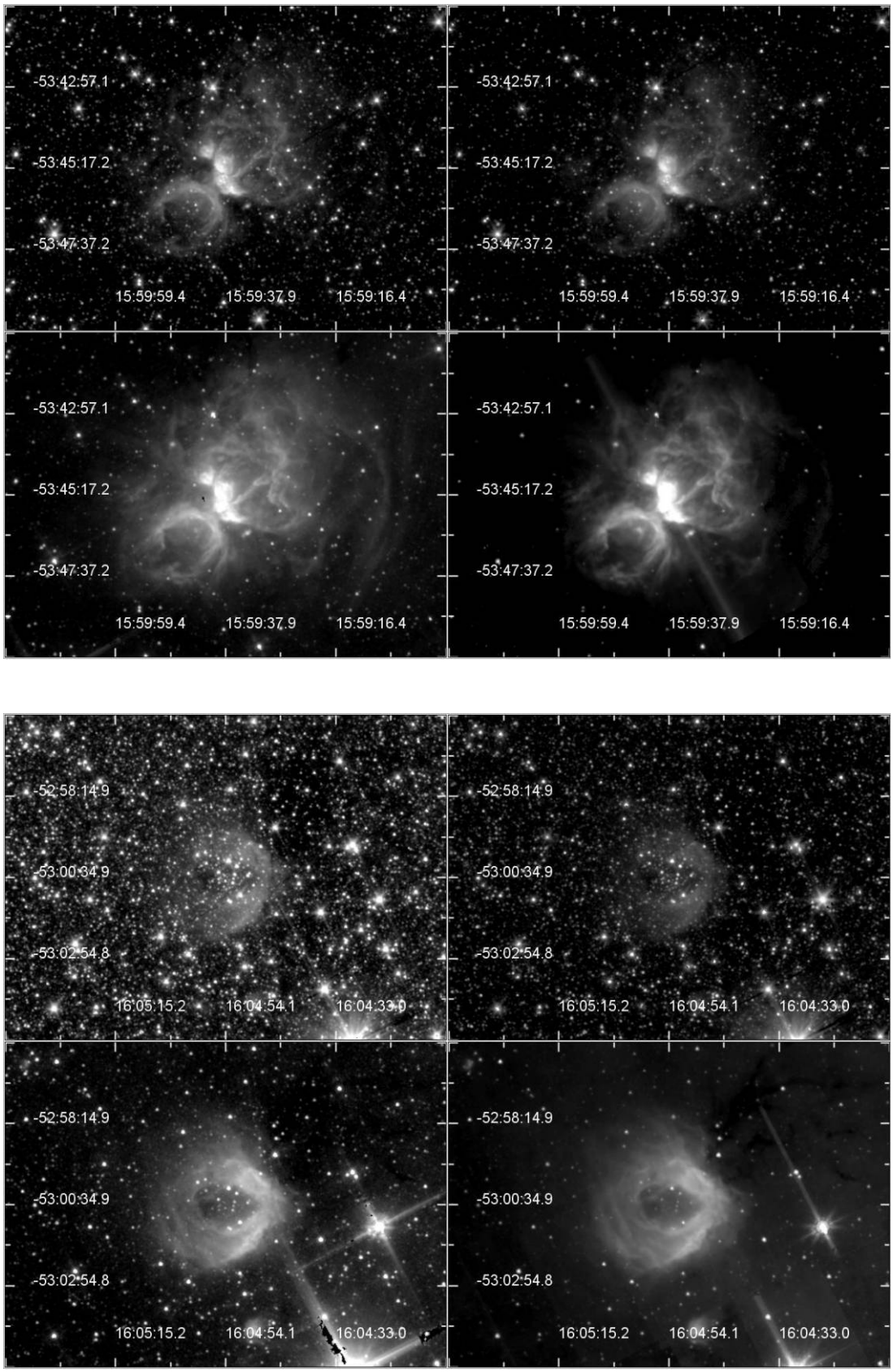

FIG. 12.— SSC IRAC images of PNG 328.5−00.5 (*top*) and PNG 329.6−00.4 (*bottom*). The order of images are arranged as Fig. 1.

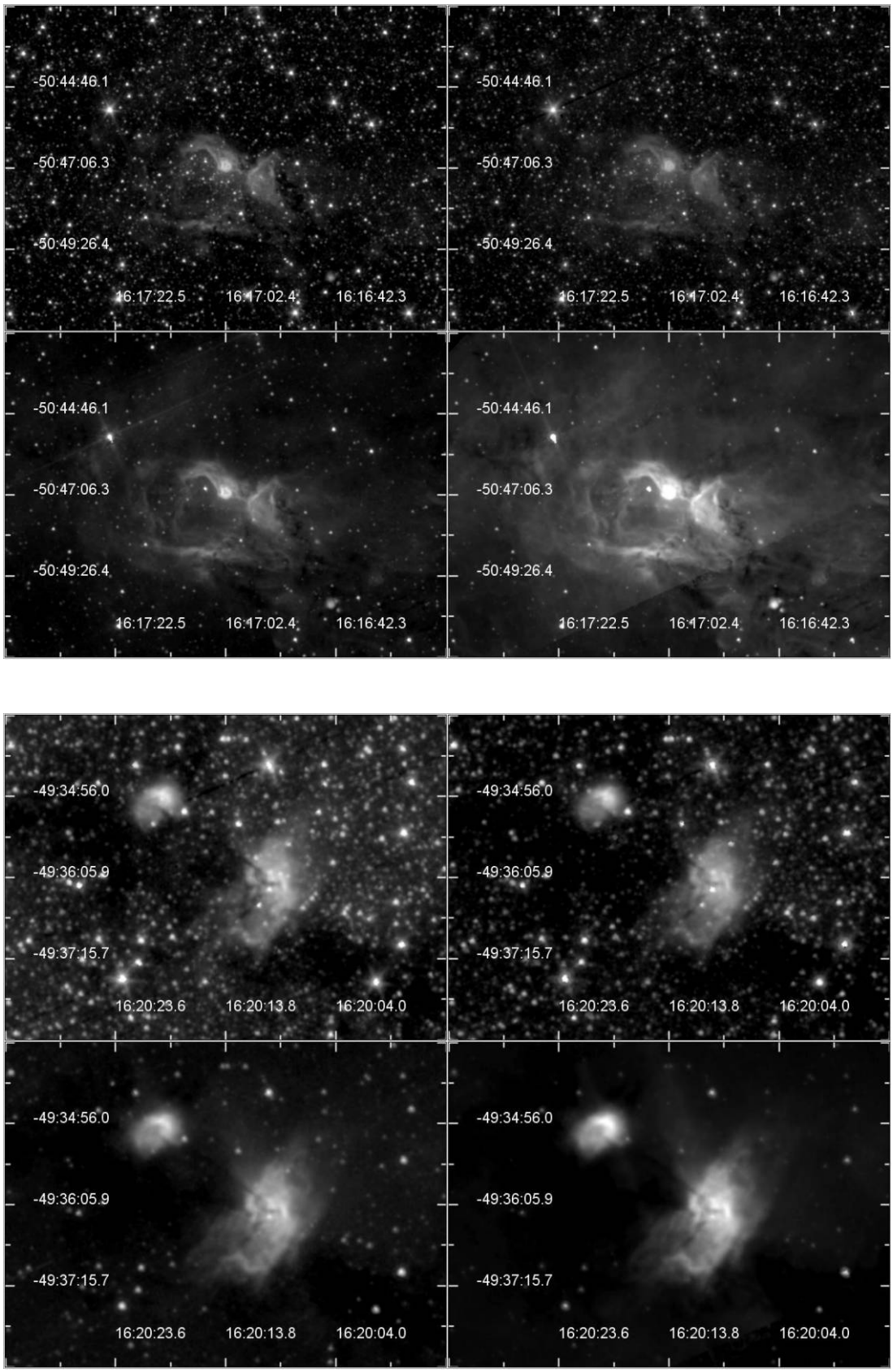

FIG. 13.—SSC IRAC images of PNG 332.5−00.1 (*top*) and PNG 333.7+00.3 (*bottom*). The order of images are arranged as Fig. 1.

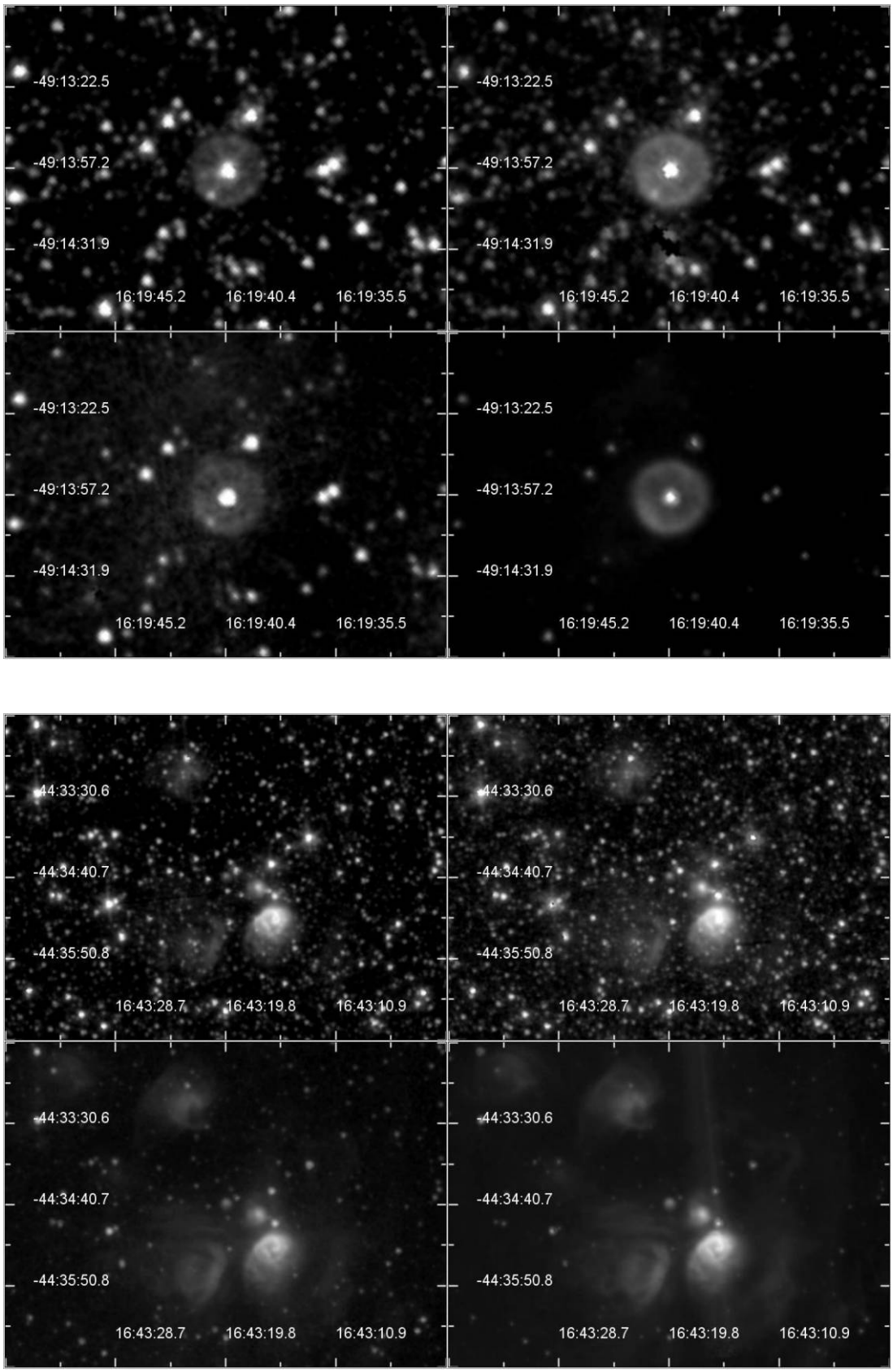

FIG. 14.—SSC IRAC images of PNG 333.9+00.6 (*top*) and PNG 340.0+00.9 (*bottom*). The order of images are arranged as Fig. 1.

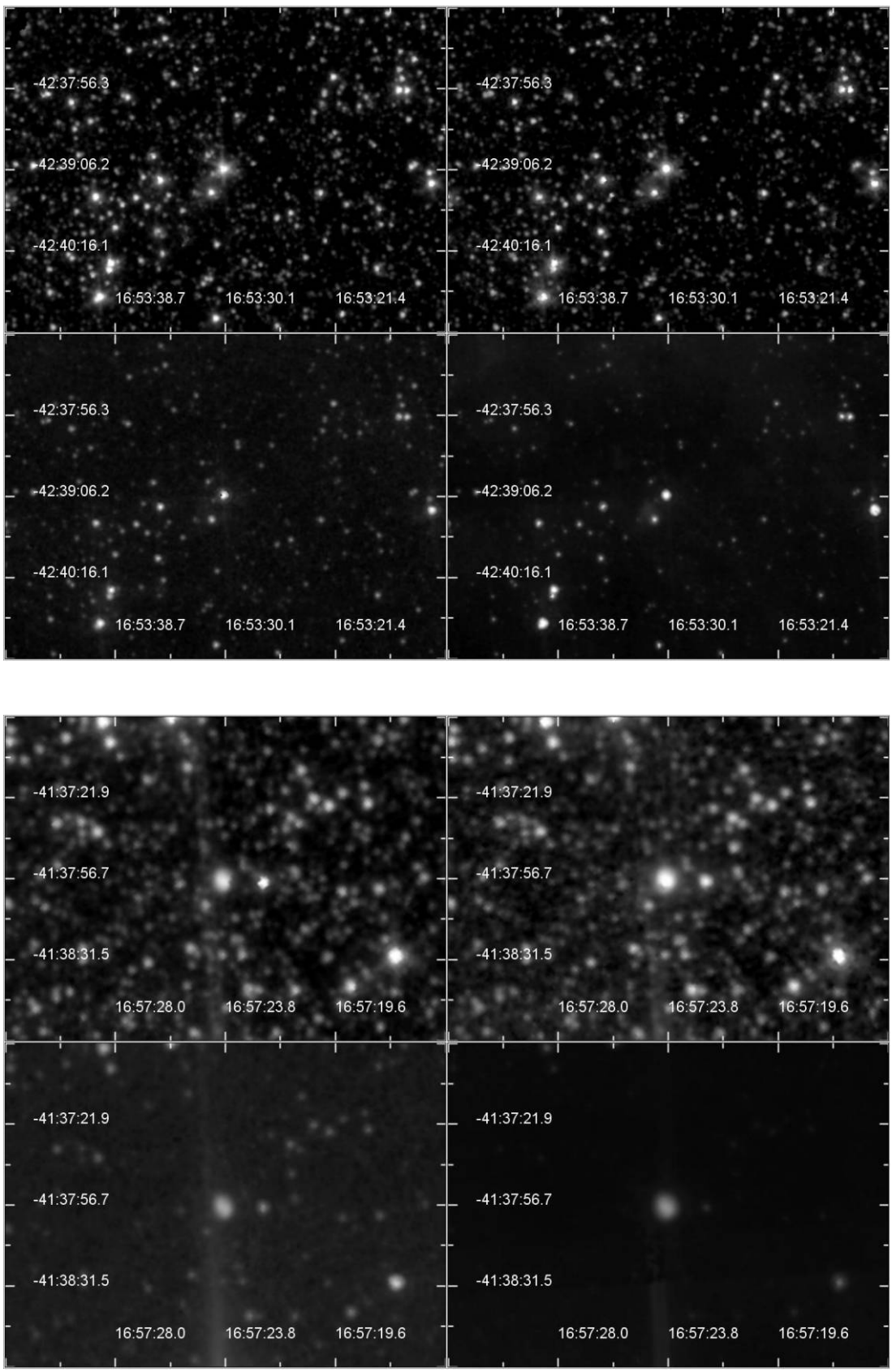

FIG. 15.—SSC IRAC images of PNG 342.7+00.7 (*top*) and PNG 343.9+00.8 (*bottom*). The order of images are arranged as Fig. 1.

TABLE 1
Spitzer IRAC Fluxes and Sizes of Detected Planetary Nebulae

Object	3.6 (mJy)	4.5 (mJy)	5.8 (mJy)	8.0 (mJy)	3.6 (arcsec)	4.5 (arcsec)	5.8 (arcsec)	8.0 (arcsec)
PNG 010.1+00.7	285	760	1307	4516	8	8	10	12
PNG 011.7−00.6	172	196	594	2023	8	8	10	12
PNG 018.6−00.0	1702	1742	14843	36825	40	60	90	120
PNG 035.5−00.4	32	48	48	141	10	10	10	10
PNG 040.3−00.4	31	26	69	180	15	20	20	20
PNG 055.5−00.5	120	137	279	1173	8	10	10	10
PNG 056.4−00.9	7.7	9.8	13.1	46.8	...	...	...	7
PNG 062.4−00.2	5	10	8	25	...	...	...	7
PNG 295.7−00.2	500	377	2764	7540	35	45	60	60
PNG 296.8−00.9	2.5	4.6	7.2	26	...	...	...	10
PNG 298.4+00.6	821	604	7423	21175	60	60	120	180
PNG 300.2+00.6	30	40	68	301	...	...	...	10
PNG 300.4−00.9	5	5	11	23	...	...	...	10
PNG 301.2+00.4	174	129	1149	3117	...	...	40 × 200	60 × 250
PNG 302.2−00.5	10	12	35	103	...	...	8 × 36	10 × 60
PNG 306.4+00.2	21	15	9	10	...	...	...	...
PNG 309.5−00.7	3213	3416	27946	69643	210 × 600	180 × 450	240 × 710	270 × 750
PNG 315.0−00.3	20	31	68	243	...	10	10	15
PNG 318.9+00.6	18	16	29	151	...	10	10	20
PNG 321.0−00.7	26	30	81	290	...	...	8 × 24	10 × 30
PNG 321.3−00.3	2486	3847	19018	36702	...	...	160 × 210	210 × 270
PNG 322.4−00.1	138	218	299	3269	...	...	...	...
PNG 328.5−00.5	31848	27238	209929	614354	180 × 360	180 × 360	360 × 540	360 × 580
PNG 329.6−00.4	2834	2760	24814	713010	...	...	220 × 400	250 × 430
PNG 332.5−00.1	9313	8132	74326	208330	72 × 280	108 × 280	120 × 430	180 × 540
PNG 333.7+00.3	2787	2737	23777	63677	60 × 90	60 × 135	90 × 180	120 × 180
PNG 333.9+00.6	35	284	167	961	30	30	45	45
PNG 340.0+00.9	...	...	...	...	20	30	50	70
PNG 342.7+00.7	245	156	119	64	...	...	...	...
PNG 343.9+00.8	95	135	200	790	...	...	10	12

wavelength ranges 2.38–45.2 μm and 40–197 μm, respectively. The aromatic infrared band (AIB) emission at 7.7 μm and the features of crystalline silicate at 15–45 μm can clearly be seen in the *ISO* spectra (Fig. 18).

Matsuura et al. (2005) presented optical and K_S band images of this PN obtained with the *Hubble Space Telescope* (*HST*) and with the infrared adaptive optics system on the Very Large Telescope (VLT), respectively. From these images they derived an extinction map that points to a compact dust structure located at the neck of the bipolar flow. The IRAC images show that the dust emission arises predominantly from the compact central region, which probably corresponds to a dust torus. Very faint emission from the symmetric lobes is seen in the IRAC 8.0 μm image only.

From the SED of this object (Fig. 16), we can see that the flux in the 8 μm band is dominated by AIB emission at 7.7 μm, with a minor contribution from the [Ne VI] line at 7.657 μm. From the 8 μm image, we can see that the AIB emission originates in a more extended region than the dust thermal emission.

4.3.2. *PNG 011.7−00.6*

PNG 011.7−00.6[=NGC 6567=IRAS 18108−1905; R.A.(J2000.0) = $18^h13^m45.0^s$, decl.(J2000.0) = $-19^\circ04'19.4''$] was detected in the DENIS, 2MASS, *MSX*, *IRAS* surveys and is detected by *Spitzer* in all four IRAC bands (Fig. 1). The NVSS survey (Condon & Kaplan 1998) gives a flux density of 163.3 ± 4.9 mJy at 1.4 GHz. NGC 6567 is an oval-shaped, type II PN. Hyung et al. (1993) presented the *IUE* spectra and obtained a low nitrogen-to-oxygen ratio of 0.14. The optical image shows that it has a diameter of 7.6″ (Acker et al. 1992, 1996). The 5.8 and 8.0 μm emissions appear to come from a more extended region.

4.3.3. *PNG 018.6−00.0*

PNG 018.6−00.0[R.A.(J2000.0) = $18^h25^m10.6^s$, decl.(J2000.0) = $-12^\circ42'28''$] was discovered in the AAO/UKST Hα and the *IRAS* surveys and is detected by *Spitzer* in all four IRAC bands (Fig. 2).

The Hα image shows a faint and cometary structure. The cometary structure, as frequently found for compact and ultracompact H II regions, is often attributed to the interaction between the ISM and stellar mass loss. Comparison between the Hα image and our IRAC image suggests that the nebula may actually have a bipolar structure with one of the optical lobes hidden due to dust obscuration. The IRAC images show an asymmetric bipolar structure with the northwestern lobe likely to be in front. Fine details such as filaments in the lobes can be seen in the IRAC images. The central star is also clearly detected. The combination of faint Hα emission and bright IR emission suggests that the object suffers from large extinction.

The SED of this object (Fig. 16) shows strong AIB emission at 7.7 μm and possibly a silicate absorption feature at 10 μm. These properties suggest that it might actually be a young stellar object (YSO) deeply embedded in a dust envelope, and indeed Parker et al. (2006) rejects this object as a PN candidate based on its morphology. Assuming this is a YSO and applying the color classification criteria of Allen et al. (2004) we can identify it as a Class I source.

TABLE 2

OTHER FLUX MEASUREMENTS

	DENIS			2MASS			*MSX*				*IRAS*			
OBJECT	*I* (mag)	*J* (mag)	*K* (mag)	*J* (mag)	*H* (mag)	*K* (mag)	8.28 μm (Jy)	12.13 μm (Jy)	14.65 μm (Jy)	21.3 μm (Jy)	12 μm (Jy)	25 μm (Jy)	60 μm (Jy)	100 μm (Jy)
PNG 010.1+00.7	12.440	10.800	9.460	10.589	10.181	9.196	3.559	5.055	17.922	35.083	7.718	58.300	189.900	166.100
PNG 011.7−00.6	12.622	11.509	10.358	11.759	11.561	10.298	1.706	2.770	4.159	4.570	2.711	7.258	<27.660	<379.000
PNG 018.6−00.0	...	...	...	...	...	...	...	...	...	...	16.200	63.910	627.100	1095.000
PNG 035.5−00.4	...	...	...	13.019	11.360	10.585	0.389	1.304	1.792	2.003	<1.821	3.552	<8.437	<211.600
PNG 040.3−00.4	...	...	...	...	...	...	...	...	...	...	2.856	0.724	<8.540	<96.500
PNG 055.5−00.5	...	...	...	11.582	11.276	10.297	1.345	4.871	10.568	19.233	4.250	32.900	20.980	58.060
PNG 056.4−00.9	...	...	...	14.205	13.712	12.760	...	...	...	...	0.504	<0.250	<0.400	<1.081
PNG 062.4−00.2	...	...	...	15.325	14.584	14.464	...	...	...	...	<1.027	0.760	7.424	<35.860
PNG 295.7−00.2	...	...	...	...	...	...	...	...	...	...	5.039	16.760	148.900	152.60
PNG 300.2+00.6	10.975	10.657	10.379	10.569	10.473	10.417	0.246	1.814	1.066	9.794	0.996	15.900	14.020	<67.560
PNG 300.4−00.9	...	...	...	15.282	13.648	13.190	...	...	...	...	...	...	...	...
PNG 302.3−00.5	15.553	14.272	13.20	14.287	13.954	13.654	0.119	1.045	...	...	...	...	...	...
PNG 306.4+00.2	10.808	10.393	9.838	10.500	10.271	9.887	...	...	...	...	...	...	...	...
PNG 315.0−00.3	16.419	15.210	...	15.221	14.735	13.552	0.238	0.254	1.493	0.907	<1.283	3.081	11.210:	<117.200
PNG 318.9+00.6	...	...	...	14.988	13.285	12.492	0.109	...	2.156	1.531	...	...	...	...
PNG 321.0−00.7	10.942	9.261	8.268	9.216	8.722	8.375	0.424	1.469	2.280	8.088	1.357	12.530	<13.630	<223.100
PNG 322.4−00.1	14.795	11.673	9.983	11.805	11.142	9.956	5.899	10.755	16.999	55.032	<16.700	70.930	35.430	<238.200
PNG 328.5−00.5	...	...	...	...	...	...	...	...	...	...	<248.100	815.300	11170.000	15900.000
PNG 333.9+00.6	13.863	10.300	8.448	10.306	9.235	8.475	0.740	4.250	4.890	10.950	4.207	19.580	33.130	<222.300
PNG 342.7+00.7	...	...	...	11.121	9.137	8.252	...	...	...	...	...	...	...	...
PNG 343.9+00.8	15.445	12.044	10.435	12.292	11.791	10.440	1.491	2.379	12.897	27.139	2.354	39.590	40.890	<69.690

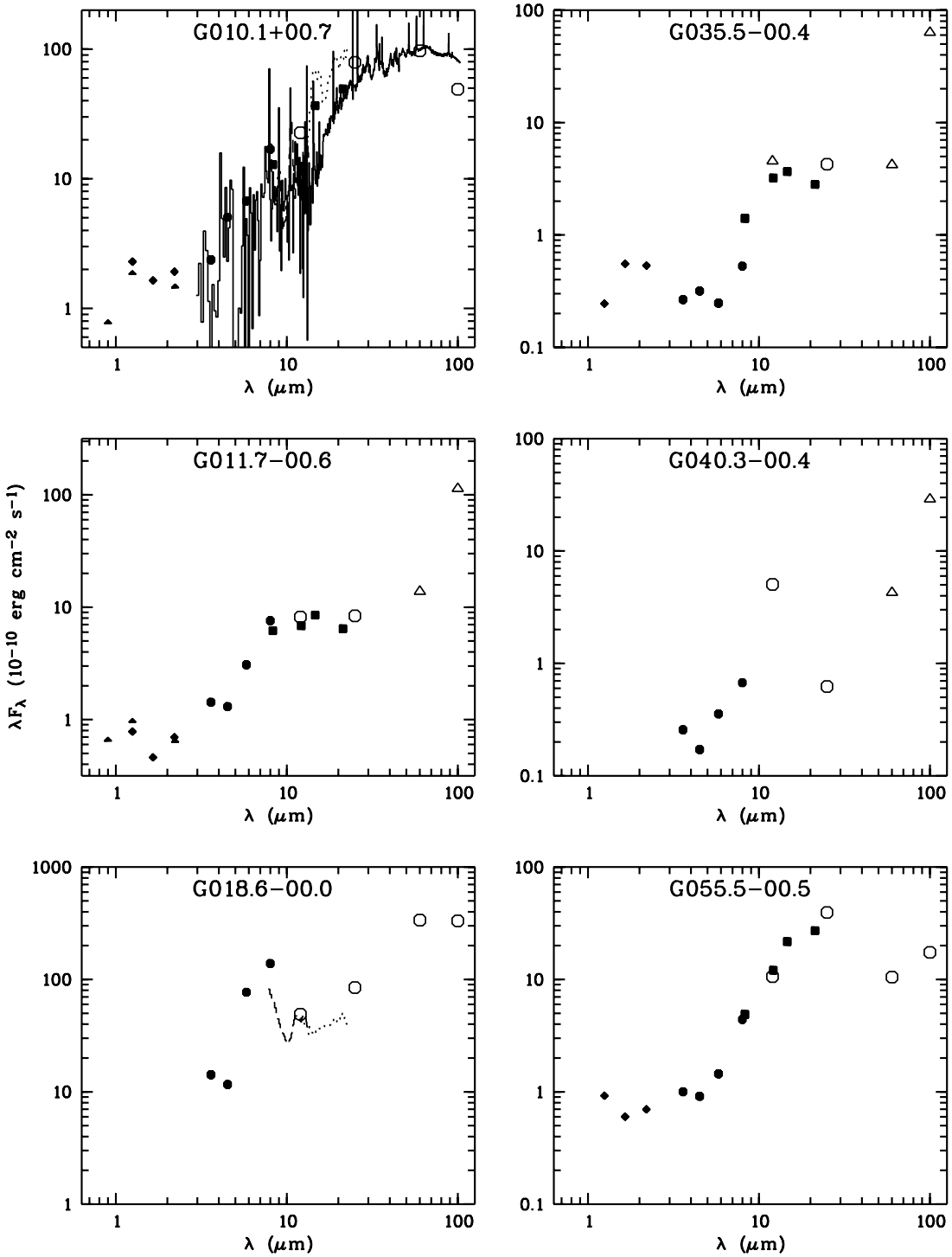

FIG. 16.— Spectral energy distributions (SEDs) of the PNs in our GLIMPSE sample. The filled triangles, filled diamonds, filled circles, open circles, and filled squares are from the DENIS, 2MASS, GLIMPSE, *IRAS*, and *MSX* surveys, respectively. The open triangles are *IRAS* upper limits. The dashed and dotted lines are *IRAS* LRS2 and LRS3 spectra, respectively. The solid lines are the *ISO* observations.

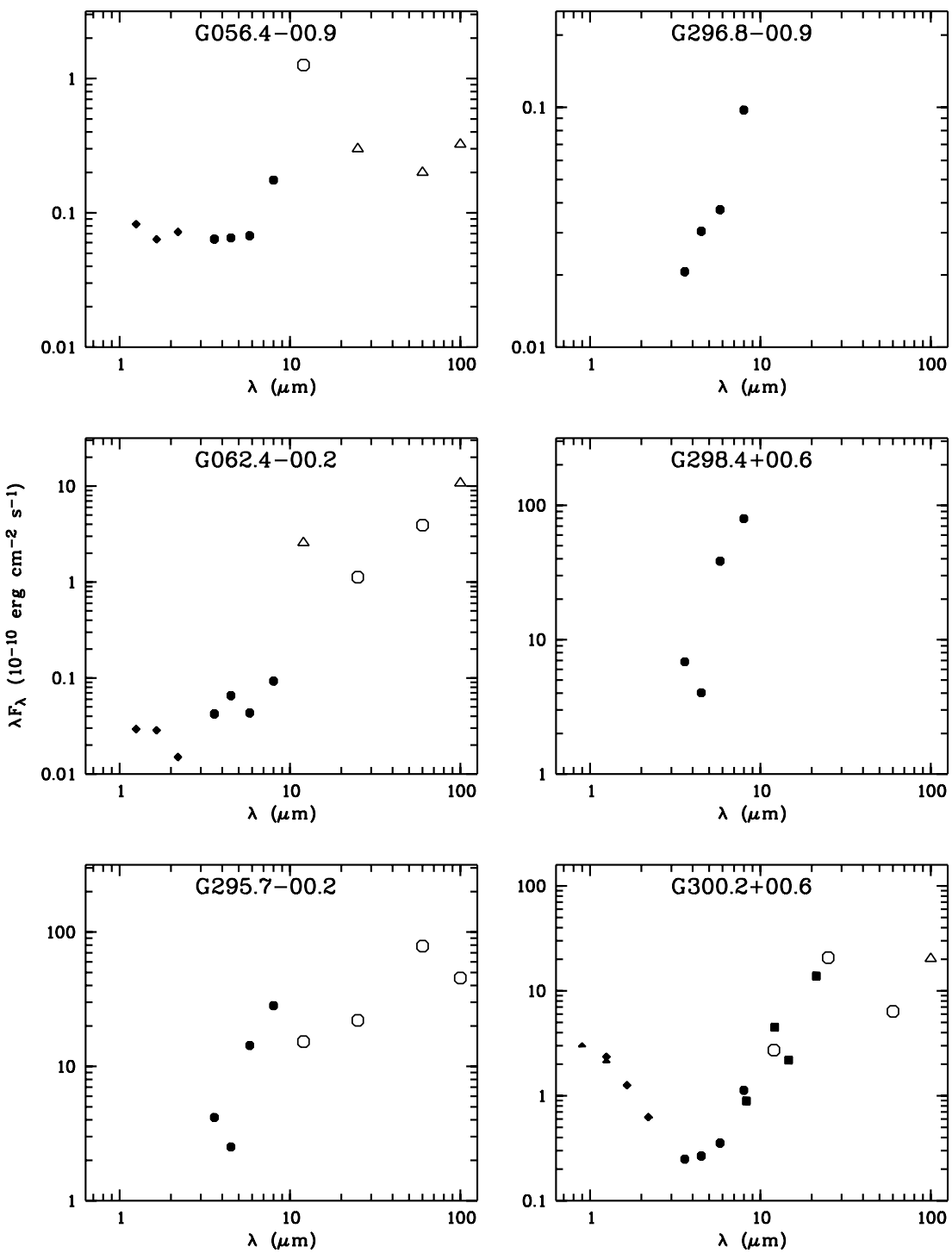

FIG. 16—*Continued*

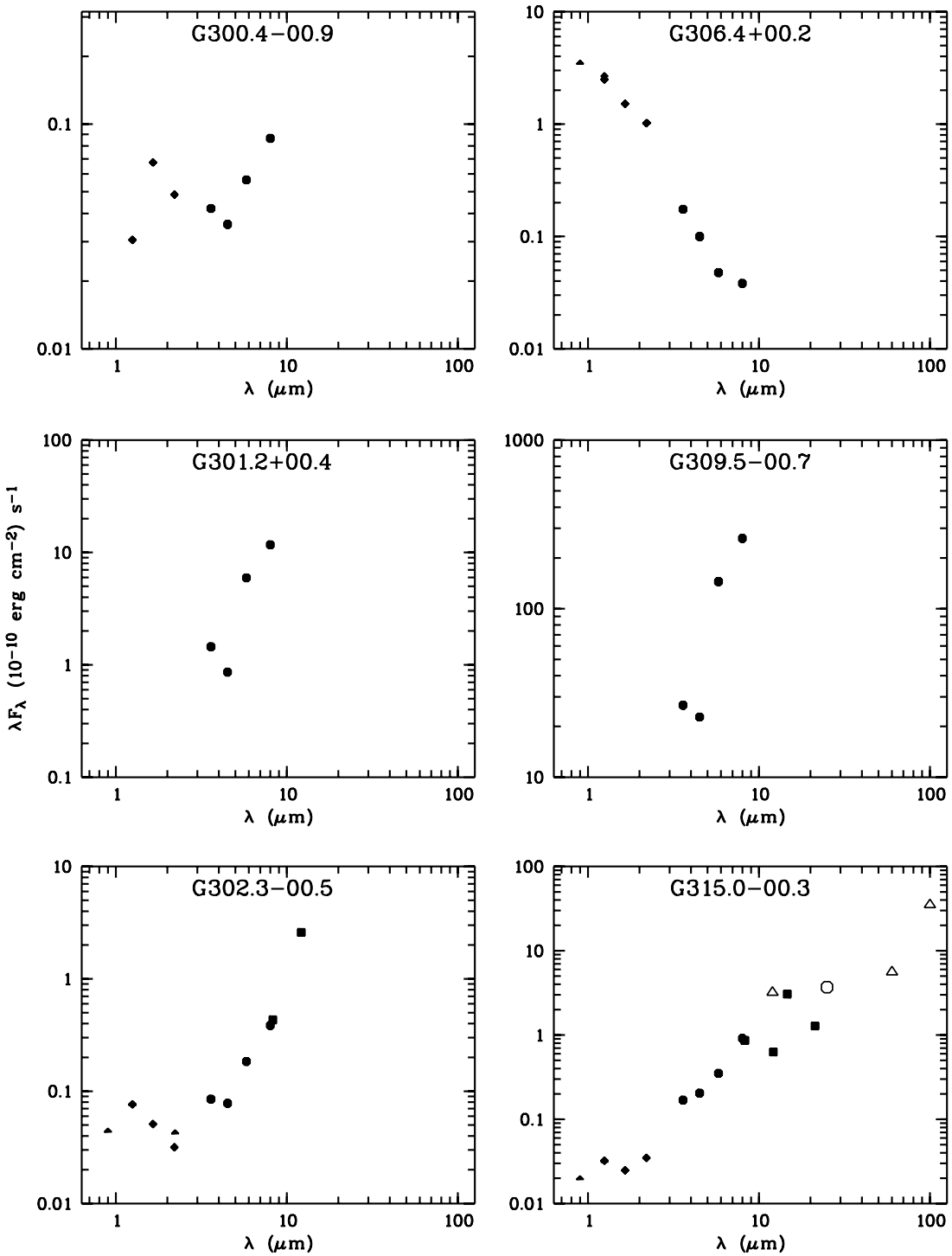

FIG. 16—*Continued*

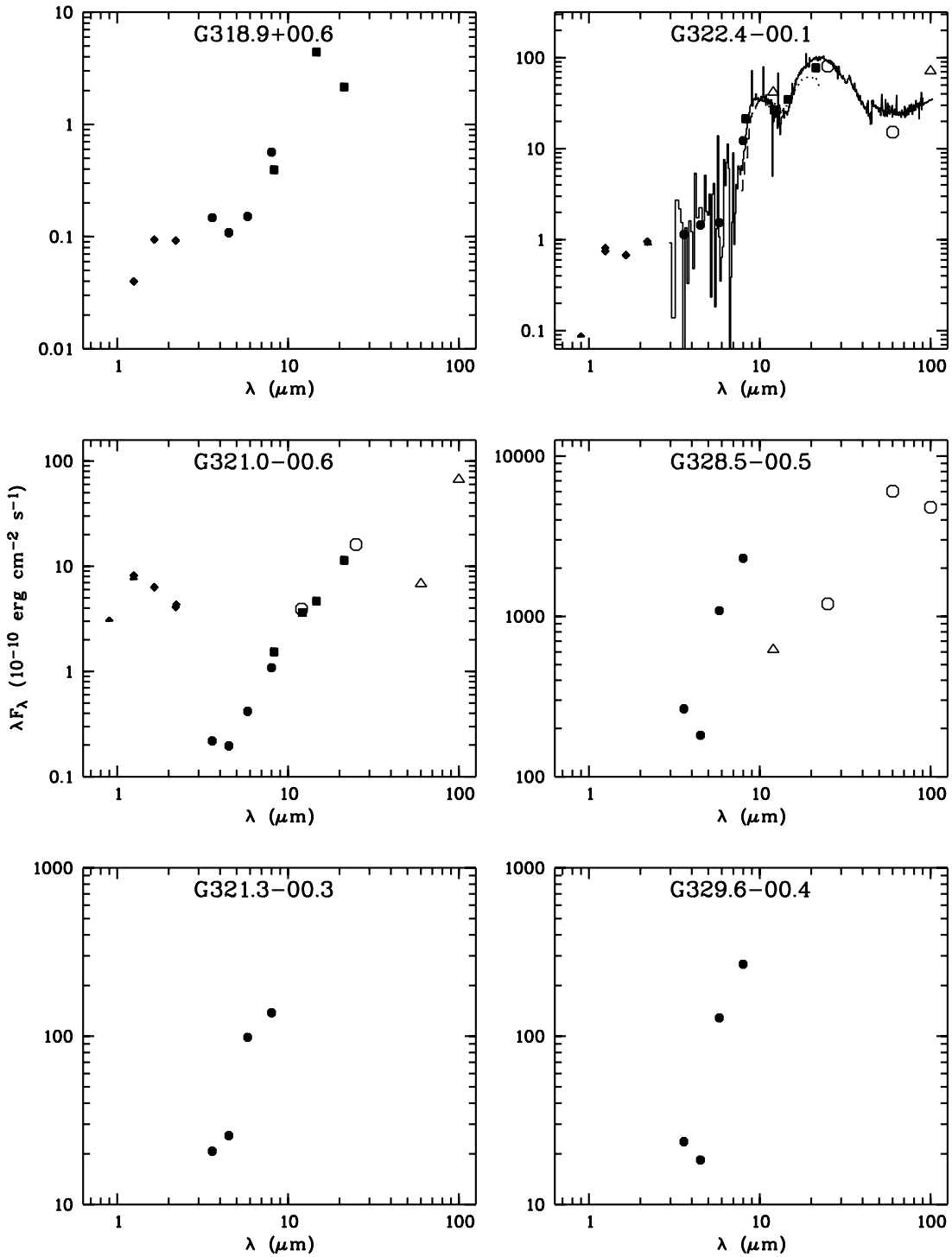

FIG. 16—*Continued*

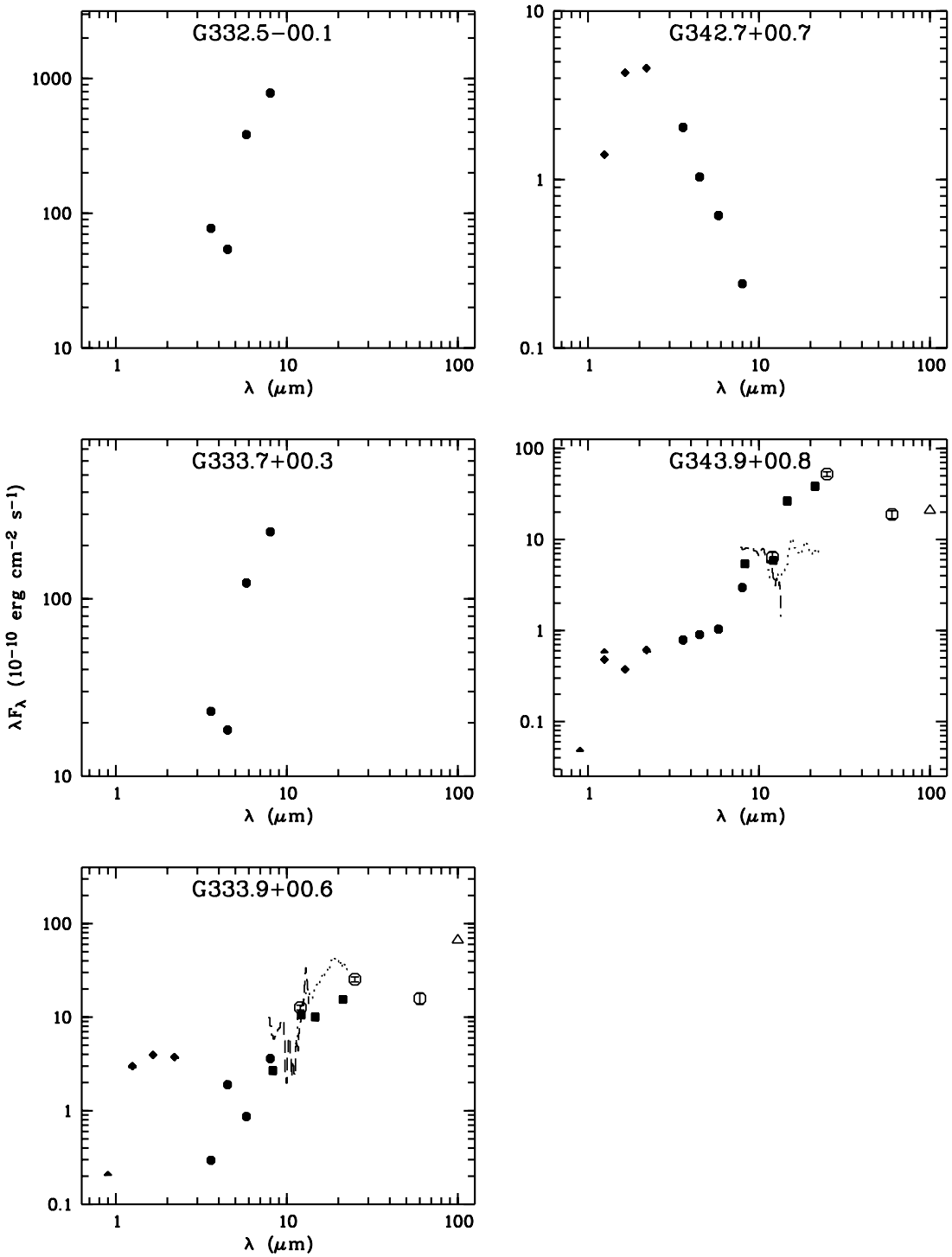

FIG. 16—*Continued*

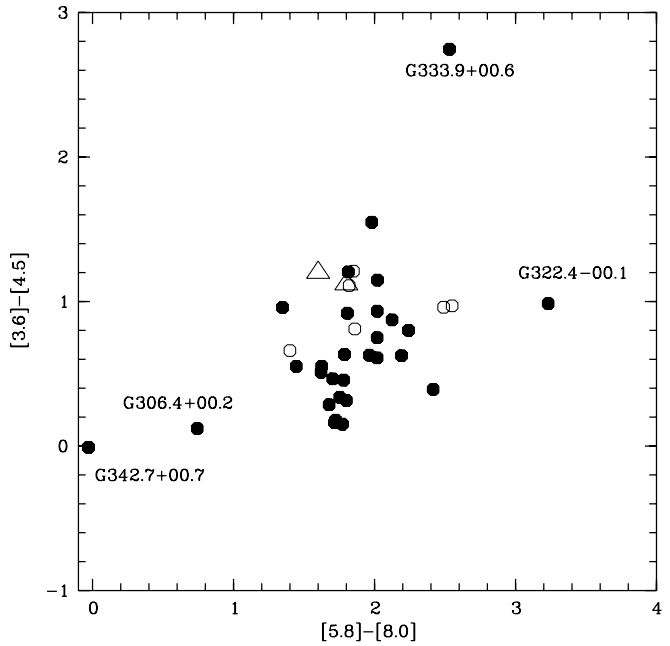

FIG. 17.—IRAC color-color plot ([3.6]−[4.5] vs. [5.8]−[8.0]) from Table 1 (*filled circles*), Hora et al. (2004, *open circles*), and Cohen et al. (2007, *open triangles*).

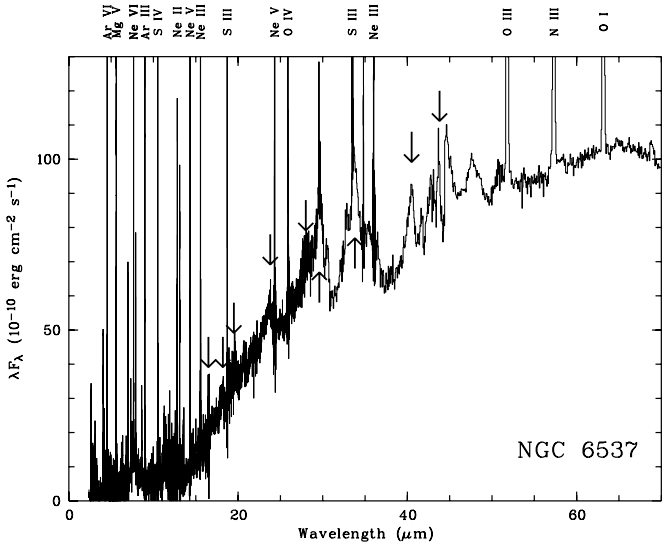

FIG. 18.—*ISO* spectrum of NGC 6537. The arrows mark the features of crystalline silicate at 16.5, 18.2, 19.5, 23.8, 28.0, 33.8, 29.6, 40.5, and 43.8 μm. A number of strong atomic lines are identified.

4.3.4. *PNG 035.5−00.4*

PNG 035.5−00.4 [IRAS 18554+0203; R.A.(J2000.0) = $18^h57^m59.5^s$, decl.(J2000.0) = +02°07′08″] was detected in the 2MASS, *MSX*, and *IRAS* surveys and is detected by *Spitzer* in all four IRAC bands (Fig. 2). According to the NVSS survey, the nebula has a flux density of 96.2 ± 3.9 mJy at 1.4 GHz (Condon & Kaplan 1998). The object was identified as a potential PN by Kistiakowsky & Helfand (1995) from near-IR observations and classified as a "likely PN" by Parker et al. (2006). The IRAC images suggests a spherical structure with a diameter of 10″. The near-IR image (Kistiakowsky & Helfand 1995) shows that the [S III] lines originate in more compact regions than the dust emission. The SED (Fig. 16) indicates a cold dust component with $T < 200$ K.

4.3.5. *PNG 040.3−00.4*

PNG 040.3−00.4 [A53=IRAS 19043+0319; R.A.(J2000.0) = $19^h06^m45.7^s$, decl.(J2000.0) = +06°23′56″] was detected in the *IRAS* survey and is detected by *Spitzer* in all four IRAC bands (Fig. 3). It shows a classical ring structure with an inner radius of ∼5″ and an outer radius of ∼10″.

4.3.6. *PNG 055.5−00.5*

PNG 055.5−00.5 [=M1-71=IRAS 19342+1935; R.A.(J2000.0) = $19^h36^m25.5^s$, decl.(J2000.0) = +19°42′30″] was detected in the 2MASS, *MSX*, and *IRAS* surveys and was detected by *Spitzer* in all four IRAC bands (Fig. 3). According to the NVSS survey, the nebula has a flux density of 84.1 ± 2.6 mJy at 1.4 GHz (Condon & Kaplan 1998). Its central star is classified by Parthasarathy et al. (1998) in the class of weak emission line stars (WELs) or [WC]−PG1159 central stars, which represent the transition stage between the [WC] central stars of PNs and the PG1159 (pre) white dwarfs. Wright et al. (2005) presented optical spectra and images of the nebula and found that it consists of a bright bulge and a faint disk extending approximately north to south. The structure is further confirmed by the IRAC 8.0 μm image. The emission from the disk is too weak to be detected in the 3.6, 4.5, and 5.8 μm images. The SED suggests the presence of cold dust ($T < 100$ K).

4.3.7. *PNG 056.4−00.9*

PNG 056.4−00.9 [=K3-42=IRAS 19373+2012; R.A.(J2000.0) = $19^h39^m35.7^s$, decl.(J2000.0) = +20°19′02″] was detected in the *IRAS* survey and was detected by *Spitzer* in all four IRAC bands (Fig. 4). The IRAC images show a very compact structure. The NVSS survey gives a flux density of 11.6 ± 0.8 mJy at 1.4 GHz (Condon & Kaplan 1998). The PN was detected by Aaquist & Kwok (1990) in their VLA radio survey of compact PNs, which gives a flux density of 19 mJy at 5 GHz. The SED suggests that the 3.6, 4.5, and 5.8 μm bands are dominated by contributions from bound-free emission, whereas the 8.0 μm band is dominated by dust emission.

4.3.8. *PNG 062.4−00.2*

PNG 062.4−00.2 [=M2-48=IRAS 19483+2546; R.A.(J2000.0) = $19^h50^m28.1^s$, decl.(J2000.0) = +25°54′22″] was detected in the 2MASS and *IRAS* surveys and was detected by *Spitzer* in the IRAC 5.8 and 8.0 μm bands only (Fig. 4). The 3.6 and 4.5 μm bands only detects the bright nucleus. The NVSS survey gives a flux density of 17.0 ± 0.7 mJy at 1.4 GHz (Condon & Kaplan 1998). Optical imaging of the object suggests the presence of bipolar outflows and bow shocks (Vázquez et al. 2000). López-Martín et al. (2002) analyzed its kinematic structure from the nebula's optical spectrum and classified it as a type I PN. The bipolar structure can clearly be seen in the IRAC 5.8 and 8.0 μm images.

4.3.9. *PNG 295.7−00.2*

PNG 295.7−00.2 [=IRAS 11467−6155; R.A.(J2000.0) = $11^h49^m13.2^s$, decl.(J2000.0) = −62°12′30″] was discovered in the AAO/UKST Hα and *IRAS* survey. It has an optical diameter of 40.7″ × 37.0″ and was detected and resolved in all four IRAC bands (Fig. 5). MacLeod et al. (1998) searched for 6.7 GHz methanol masers for a *IRAS*-selected sample and did not detect methanol masers in this object. The IRAC images show that the object is composed of two bright lobes embedded in a diffuse nebula with extended tails in the north and west directions. The Hα image, however, only reveals a compact emission region. Based on

the *IRAS* fluxes, Whiteoak (1992) identified it as a compact H II region. Parker et al. (2006) rejects this object as a PN candidate based on its morphology.

4.3.10. *PNG 296.8−00.9*

PNG 296.8−00.9 [R.A.(J2000.0) = $11^h57^m3.1^s$, decl.(J2000.0) = $-63^\circ12'43''$] was discovered in the AAO/UKST Hα survey. It has an optical diameter of $13'' \times 11''$ and was detected by *Spitzer* in the IRAC 5.8 and 8.0 μm bands only (Fig. 5). The Hα image shows a spiral structure, which, however, is not resolved in the IRAC images. The SED shows a very steep rise between the 5.8 and 8.0 μm bands, which could be due to strong AIB emissions at 7.7 μm.

4.3.11. *PNG 298.4+00.6*

PNG 298.4+00.6 [R.A.(J2000.0) = $12^h13^m09.0^s$, decl.(J2000.0) = $-61^\circ50'28''$] was discovered in the AAO/UKST Hα survey. It has an optical diameter of $24''$. This object is very red in the GLIMPSE field and was detected by *Spitzer* in the IRAC 4.5, 5.8, and 8.0 μm bands (Fig. 6). While the Hα image shows an approximately spherical structure, the IRAC images suggest that the dust emission is distributed in two bipolar lobes with some filaments in the outer diffuse regions.

4.3.12. *PNG 300.2+00.6*

PNG 300.2+00.6 [He 2-83=IRAS 12259−6148; R.A.(J2000.0) = $12^h28^m45.6^s$, decl.(J2000.0) = $-62^\circ05'35''$] was detected by the DENIS, 2MASS, *MSX*, and *IRAS* surveys and was detected in all four IRAC bands (Fig. 7).

The IRAC images show a spherical structure with a diameter of $10''$. Górny et al. (1999) presented optical images of this PN, showing a similar appearance and size with those in the IRAC images. The SED (Fig. 16) shows the presence of cold dust ($T < 100$ K) and a red companion star.

4.3.13. *PNG 300.4−00.9*

PNG 300.4−00.9 [=He 2-84; R.A.(J2000.0) = $12^h28^m46.7^s$, decl.(J2000.0) = $-63^\circ44'35''$] is a medium-excitation bipolar PN with a narrow waist. The nebula has an optical diameter of $38'' \times 30''$ and is detected in the IRAC 4.5, 5.8, and 8.0 μm bands (Fig. 7). The PN was detected in the 2MASS survey but not included in the DENIS point source catalog due to its extended size. The optical images in Corradi & Schwarz (1993) and Górny et al. (1999) show a distorted point symmetrical structure. The IRAC images show that dust emission originates predominantly in the bright waist. The faint extended emission was detected in the 8.0 μm band only.

4.3.14. *PNG 301.2+00.4*

PNG 301.2+00.4 [R.A.(J2000.0) = $12^h37^m09.6^s$, decl.(J2000.0) = $-62^\circ23'10''$] was discovered in the AAO/UKST Hα survey. It has an optical diameter of $15.3'' \times 12.9''$. This object is very red in the GLIMPSE field and is detected by *Spitzer* in the IRAC 4.5, 5.8, and 8.0 μm bands (Fig. 7). The Hα image shows a faint elliptical appearance, whereas the IRAC images shows a much more extended and bright structure. It is worth noting that an extended filament structure to the north of the PN appears in the GLIMPSE field but has no corresponding feature in the Hα image. The difference between the IRAC and Hα images represents the different spatial distributions of dust and ionized gas.

4.3.15. *PNG 302.3−00.5*

PNG 302.3−00.5 [R.A.(J2000.0) = $12^h46^m27.1^s$, decl.(J2000.0) = $-63^\circ24'22''$] was discovered in the AAO/UKST Hα, DENIS, 2MASS, and *MSX* surveys. It has an optical diameter of $22'' \times 15''$ and was detected in the IRAC 5.8 and 8.0 μm bands (Fig. 8). According to the MASH catalog, Hβ has a much larger flux than the [O III] λ5007 line, suggesting that the PN belongs to an extremely low excitation class. The Hα image shows a very elliptical appearance and thus was classified as a bipolar PN by Parker et al. (2006). However, the IRAC images show an edge-on ringlike structure, which is probably a better description of its morphology. The SED (Fig. 16) suggests the presence of cold dust ($T < 150$ K).

4.3.16. *PNG 306.4+00.2*

PNG 306.4+00.2 [R.A.(J2000.0) = $13^h22^m5.5^s$, decl.(J2000.0) = $-62^\circ24'6''$] was discovered in the AAO/UKST Hα, DENIS and 2MASS surveys and was detected by *Spitzer* in all four IRAC bands (Fig. 8). Both the Hα and IRAC images show the extended bipolar structure and bright central star. The diffuse nebula is much fainter than the central compact region. The SED (Fig. 16) probably represents the measurements of the central object.

4.3.17. *PNG 309.5−00.7*

PNG 309.5−00.7 [R.A.(J2000.0) = $13^h49^m52.1^s$, decl.(J2000.0) = $-62^\circ49'41''$] was detected by *Spitzer* in all four IRAC bands (Fig. 9). This object is very red in the GLIMPSE field and has a large size. The IRAC images show a cometary appearance, implying the interaction between the nebula and the ISM. This object is classified as an interstellar bubble based on its morphology and is given the catalog number of S141 (where the prefix S stands for south, not to be confused with objects in the Sharpless catalog, Churchwell et al. 2006). Parker et al. (2006) rejects this object as a PN candidate based on its morphology. We note that there is a separate extended source southwest of the main nebula and has a similar color to PNG 309.5−00.7. From the morphology of this smaller nebula, it could be considered as a PN candidate.

4.3.18. *PNG 315.0−00.3*

PNG 315.0−00.3 [=He 2-111=Wray 16-156=Sa 2-106=IRAS 14295−6036; R.A.(J2000.0) = $14^h33^m18.2^s$, decl.(J2000.0) = $-60^\circ49'44.2''$] was discovered in the DENIS, 2MASS, *MSX*, and *IRAS* surveys and is detected by *Spitzer* in all four IRAC bands (Fig. 9). The *ISO* and *IUE* spectra were presented by Pottasch et al. (2000). It is a high-excitation type I PN and has an abnormally high helium abundance (He/H = 0.25; Perinotto et al. 2004). Both the optical (Corradi & Schwarz 1995) and IRAC images show a bipolar structure. The SED (Fig. 16) suggests that the IR emission is dominated by thermal process of cold dust with $T < 100$ K.

4.3.19. *PNG 318.9+00.6*

PNG 318.9+00.6 [R.A.(J2000.0) = $14^h57^m35.5^s$, decl.(J2000.0) = $-58^\circ12'16''$] was discovered in the AAO/UKST Hα, 2MASS, and *MSX* surveys. It has an optical diameter of $27.2'' \times 13.6''$ and was detected and resolved by *Spitzer* in all four IRAC bands (Fig. 10). Both the Hα and IRAC images show a elliptical structure. The SED (Fig. 16) show that the 8.0 μm flux is much larger than those of the other bands. This could be the result of contribution from the 7.7 μm AIB feature, or the transition to strong cold dust emission longward of this wavelength.

At first we found that the 4.5 μm flux of this object to be anomalously low. This is due to the fact that there is a bright point source in the 4.5 μm band (14 mJy) that is not detected in any of the other bands. Since the extended flux is determined by an on-off subtraction process, there could be an oversubtraction due to the presence of this point source. We decided to artificially add back 14 mJy to the 4.5 μm extended flux, which leads to an apparently more reasonable SED.

4.3.20. *PNG 321.0−00.7*

PNG 321.0−00.7 [=IRAS 15127−5811; R.A.(J2000.0) = $15^h16^m40.9^s$, decl.(J2000.0) = $-58^\circ22'26''$] was discovered in the AAO/UKST Hα, DENIS, 2MASS, *MSX*, and *IRAS* surveys. It has an optical diameter of $17.0'' \times 10.2''$ and is detected and resolved by *Spitzer* in all four IRAC bands (Fig. 11). Both the Hα and IRAC images show an elliptical structure. The central compact core is clearly detected by the 3.6, 4.5, and 5.8 μm bands. The SED (Fig. 16) shows a clear separation between the photospheric and dust components with the dust component beginning to dominate around 4 μm.

4.3.21. *PNG 321.3−00.3*

PNG 321.3−00.3 [R.A.(J2000.0) = $15^h17^m30.0^s$, decl.(J2000.0) = $-57^\circ50'59''$] was discovered in the AAO/UKST Hα survey. It has an optical diameter of $112'' \times 97''$ and is detected and resolved by *Spitzer* in all four IRAC bands (Fig. 11). The Hα image shows a very faint and approximately circular structure. The object is very red, and the nebular structure is clearly defined by dust emission seen in the IRAC images. This object is classified as an interstellar bubble based on its morphology and is given the catalog number of S89 (Churchwell et al. 2006).

4.3.22. *PNG 322.4−00.1*

PNG 322.4−00.1 [=Hen 2-124=Pe 2-8=Sa 3-28=IRAS 15198−5758; R.A.(J2000.0) = $15^h23^m43.5^s$, decl.(J2000.0) = $-57^\circ09'28''$] was discovered in the AAO/UKST Hα, DENIS, 2MASS, *MSX*, and *IRAS* surveys. It has an optical diameter of $32.0'' \times 15.1''$ and is detected and resolved by *Spitzer* in all four IRAC bands (Fig. 11). The *IJK* photometry of the PN with DENIS has been presented by Schmeja & Kimeswenger (2002). It is a low-excitation PN. No X-ray emission is detected (Guerrero et al. 2000). The Hα image shows an elongated structure, whereas the object in the IRAC images is compact. From the SED (Fig. 16), the 3.6, 4.5, and 5.8 μm band fluxes are consistent with nebular bound-free emission, with the dust emission dominating in the 8.0 μm band.

The *ISO* spectrum of this object (Fig. 19) shows strong amorphous silicate emission features at 10 and 18 μm. The 8.0 μm image in Figure 11, therefore, traces the spatial distribution of amorphous silicates.

4.3.23. *PNG 328.5−00.5*

PNG 328.5−00.5 [=IRAS 15557−5337; R.A.(J2000.0) = $15^h59^m38.2^s$, decl.(J2000.0) = $-53^\circ45'32''$] was discovered in the AAO/UKST Hα, DENIS, 2MASS, *MSX*, and *IRAS* surveys. It has an optical diameter of $220''$ and is detected and resolved by *Spitzer* in all four IRAC bands (Fig. 12). The object is very red and is saturated in the 8.0 μm band. Both the Hα and IRAC images show a clear bipolar structure with a tight waist. More details are revealed by the IRAC images, which clearly show the symmetric polar outflow filaments. Parker et al. (2006) rejects this object as a PN candidate based on its morphology. Given its large size and red color, it could be an H II region. No methanol maser was detected for the object (MacLeod et al. 1998).

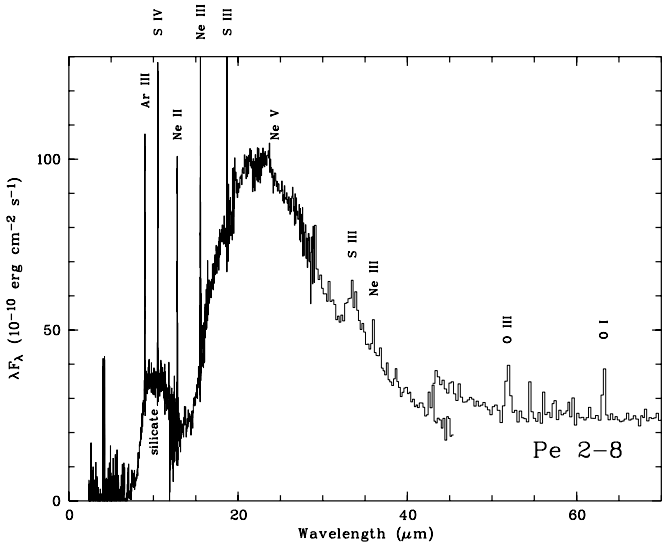

FIG. 19.—*ISO* spectrum of Pe 2-8 (PNG 322.4−00.1). A number of strong atomic lines are identified above the panel.

4.3.24. *PNG 329.6−00.4*

PNG 329.6−00.4 [R.A.(J2000.0) = $16^h04^m52.8^s$, decl.(J2000.0) = $-53^\circ00'32''$] was discovered in the AAO/UKST Hα, DENIS, 2MASS, and *MSX* surveys. It has an optical diameter of $75'' \times 155''$ and is detected and resolved by *Spitzer* in all four IRAC bands (Fig. 12). The Hα images show a compact nucleus with extremely faint extended emission. The IRAC images show a clear ringlike structure. Parker et al. (2006) rejects this object as a PN candidate based on its morphology. Its appearance and IR color are very similar with those of PNG 321.3−00.3, suggesting the two objects may share some common evolutionary origins. Indeed, both objects are in the catalog of interstellar bubbles of Churchwell et al. (2006) with PNG 329.6−00.4 given the designation of S69.

4.3.25. *PNG 332.5−00.1*

PNG 332.5−00.1 [R.A.(J2000.0) = $16^h16^m56.4^s$, decl.(J2000.0) = $-50^\circ47'23''$] was discovered in the AAO/UKST Hα, DENIS, 2MASS, and *MSX* surveys. The nebula has an optical diameter of $34''$ and shows a faint and approximately spherical structure. The nebula is detected and resolved by *Spitzer* in all four IRAC bands (Fig. 13) and shows a much larger and more detailed structure than in the optical image. The object is very red with a clear bipolar structure with some filamentary structures. It is possible that the faint and spherical structure in the Hα image represents the central region of the nebula. Parker et al. (2006) rejects this object as a PN candidate based on its morphology.

4.3.26. *PNG 333.7+00.3*

PNG 333.7+00.3 [R.A.(J2000.0) = $16^h20^m09.6^s$, decl.(J2000.0) = $-49^\circ35'52''$] was discovered in the AAO/UKST Hα, 2MASS, and *MSX* surveys. It has an optical diameter of $11.5'' \times 9.5''$ and has a diffuse outer structure. The object is very red and shows an elliptical structure in all four IRAC bands. In the IRAC images there is a bright extended source with similar IR colors in the NE of the object. The two may be related.

4.3.27. *PNG 333.9+00.6*

PNG 333.9+00.6 [=PM 5=IRAS 16159−4906; R.A.(J2000.0) = $16^h19^m40.16^s$, decl.(J2000.0) = $-49°13'59.7''$] was discovered in the AAO/UKST Hα, DENIS, 2MASS, DENIS, and *IRAS* survey. Optical spectra of the object were observed with the SAAO 1.9 m and MSSSO 2.3 m telescopes and the object is identified as a PN with a [WN] central star (Morgan et al. 2003). It has an optical diameter of 32″ and is detected and resolved in all four IRAC bands (Fig. 14). The Hα and IRAC images show similar structures of a bright central star surrounded by a spherical shell.

The bright IR emission in the central region can be attributed to bound-free emission from the circumstellar ionized gas. Dust emission begins to dominate at 8 μm and is mostly distributed in the shell.

4.3.28. *PNG 340.0+00.9*

PNG 340.0+00.9 [R.A.(J2000.0) = $16^h43^m16.09^s$, decl.(J2000.0) = $-44°35'19''$] was discovered in the AAO/UKST Hα survey and is detected in all four IRAC bands (Fig. 14). The object is very red and almost invisible in the Hα image. There are three other very red extended sources in the IRAC images that may be related to the PN. Due to the presence of multiple extended components, the total flux is difficult to determine for this object and the corresponding entry is therefore absent in Table 1.

4.3.29. *PNG 342.7+00.7*

PNG 342.7+00.7 [=H1-3; R.A.(J2000.0) = $16^h53^m31.43^s$, decl.(J2000.0) = $-42°39'18''$] was discovered in the AAO/UKST Hα and 2MASS surveys and is detected in all four IRAC bands (Fig. 15). It is a low-excitation PN. The Hα image shows an approximately elliptical structure with a distorted tail, whereas the IRAC images only show a compact nucleus. No diffuse dust emission is detected. The object has a starlike SED (Fig. 16) with a color temperature of $\sim$150 K.

4.3.30. *PNG 343.9+00.8*

PNG 343.9+00.8 [=H1-5=IRAS 16538−4133; R.A.(J2000.0) = $16^h57^m23.7^s$, decl.(J2000.0) = $-41°37'56''$] was discovered in the AAO/UKST Hα, DENIS, 2MASS, *MSX*, and *IRAS* surveys is detected in all four IRAC bands (Fig. 15). It is a medium-excitation PN. Both the Hα and IRAC images show a elliptical structure. The SED implies the presence of cold dust with a temperature of $\sim$100 K.

4.4. *Nondetections*

A number of PNs have no obvious counterparts in the GLIMPSE fields. Their names are listed below, and no further analysis was done on these objects: PNG 010.2+00.3, PNG 011.5+01.0, PNG 011.7−00.0, PNG 014.6+01.0, PNG 015.5−01.0, PNG 015.5−00.0, PNG 016.4−00.9, PNG 017.2+00.1, PNG 019.9+00.9, PNG 020.2−00.6, PNG 020.9+00.8, PNG 021.7−00.6, PNG 021.8−00.4, PNG 021.2+00.9, PNG 023.4+00.7, PNG 023.5−00.1, PNG 025.9−00.9, PNG 033.9−00.9, PNG 033.4+00.1, PNG 033.1+00.2, PNG 031.9−00.3, PNG 031.3−00.5, PNG $031.3-00.5_2$, PNG 030.5−00.2, PNG 030.0+00.0, PNG 029.8+00.5, PNG 029.5+00.6, PNG 029.2−00.0, PNG 029.0+00.4, PNG $029.0+00.4_2$, PNG 028.9+00.2, PNG 028.8−00.2, PNG 028.7−00.3, PNG 027.7+00.7, PNG 027.7−00.6, PNG 027.6−00.8, PNG 027.4−00.9, PNG 026.9−00.7, PNG 026.8−00.5, PNG 025.9−00.9, PNG 041.2−00.6, PNG 060.5−00.3, PNG 295.9−00.4, PNG 296.2−00.4, PNG 299.1−00.1, PNG 299.7+00.1, PNG 302.6−00.9, PNG 302.7−00.9, PNG 303.3+00.0, PNG 303.6+00.5, PNG 308.4+00.4, PNG 309.5+00.8, PNG 310.0+00.3, PNG 310.6+00.2, PNG 311.7−00.9, PNG 312.1+00.3, PNG 312.2+00.1, PNG 312.8+00.2, PNG 314.6−00.1, PNG 314.9+00.5, PNG 315.9+00.3, PNG 317.5+00.8, PNG 331.2+00.0, PNG 332.3−00.9, PNG 333.2−00.6, PNG 334.0+00.7, PNG 336.0−00.4, PNG 337.3+00.6, PNG 337.4+00.3, PNG 337.6+00.7, PNG 338.1+00.4, PNG 339.1+00.9, PNG 339.9+00.5, PNG 340.3−00.5, PNG 340.8+00.8, PNG 343.3−00.6, PNG 345.4+00.1, PNG 346.9−00.0, PNG 347.0+00.3, PNG 347.2−00.8.

These PNs are not detected possibly for a variety of reasons. For some large objects (e.g., PNG 029.8+00.5, which is over 1′ in size), the dust emission is probably just too diffuse to be seen. Others (e.g., PNG 302.7−00.9) lie in areas of general diffuse emission on the Galactic plane and are difficult to identify.

In several cases, there are nearby point sources that have a rising flux distribution from 3.8 to 8.0 μm, similar to that of PNs. For example, there is a point source ($l = 302.6125$, $b = -0.963673$) near PNG 302.6−00.9 with fluxes of 3.358, 7.664, 12.38, and 24.87 mJy at 3.6, 4.5, 5.8, and 8.0 μm, respectively. Other examples are a point source at $l = 312.294$, $b = 0.0979$ near PNG 312.2+00.1 with fluxes 10.1, 7.241, 15.41, and 47.59 mJy, and a point source at $l = 312.877$, $b = 0.232405$ near PNG 312.8+00.2 with fluxes of 16.7, 28.56, 49.12, 64.19 mJy. In all cases, no extended emission is found.

4.5. *Object Classification*

Although our sample objects are selected from the PN catalog, we have to bear in mind that the PN designation is not certain without a complete spectral coverage. At the most elementary level, PNs can be separated from compact H II regions by the relative strengths of the Hα and [O III] lines (PNs have stronger [O III] lines), and their respective infrared colors (H II regions usually having redder colors). In terms of morphology, PNs usually process a greater degree of symmetry and less diffuse in appearance. But these guidelines are not foolproof, and confusion between these two classes of objects is always a problem.

We have also detected a number of objects that bear PNG designations and are therefore emission-line objects. However, based on their infrared morphology, they are unlikely to be PNs. An analysis of these objects (listed below) will be presented in a separate paper: PNG 013.8+00.2, PNG 024.4+00.4, PNG 035.1−00.7, PNG 033.3+00.7, PNG 033.2+00.7, PNG 027.3−00.1, PNG 025.3−00.1, PNG 297.3−00.2, PNG 297.4−00.7, PNG 297.6−00.9, PNG 298.1−00.7, PNG 298.2−00.3, PNG 303.1−00.9, PNG 331.4+00.5, PNG 333.6−00.2, PNG 338.9−00.0.

5. DISCUSSION

Since the IRAC band passes are broad, both line and continuum emissions contribute to the fluxes observed in our sample. In the 5–8 μm region, contribution to the continuum emission includes bound-free emission from the ionized nebula and thermal emission from dust. Emission lines, both atomic and molecular, are prominent in the spectrum of PNs. In particular, a number of strong AIB (e.g., 3.3, 6.2, and 7.7 μm) emission features lie in the IRAC 3.6, 5.8, and 8.0 μm bands, respectively. Since AIB emissions are common in carbon-rich PNs, we can only be certain that the 4.5 μm band is free from AIB contributions. For oxygen-rich PNs, strong amorphous silicate emission features are expected to be present, and the 9.7 μm amorphous silicate feature can contribute to the IRAC 8.0 μm band. Since both the AIB and silicate features (together with their associated underlying continua) can be

considered as solid-state features, we will group them together and label such emissions as "dust" emission.

Examples of contributions from atomic lines to the IRAC bands include H Brα at 4.05 μm to the 4.5 μm band, [Ar II] at 6.98 μm and [Ar III] at 8.99 μm to the IRAC 8.0 μm band (Hora et al. 2004). Furthermore, a number of rotational transitions in the ground vibrational state of molecular hydrogen lie within the IRAC bands. Examples include $S(4)$ at 8.025 μm, $S(5)$ at 6.909 μm, $S(6)$ at 6.109 μm, $S(7)$ at 5.511 μm, $S(8)$ at 5.053 μm, $S(9)$ at 4.695 μm, $S(10)$ at 4.410 μm, and $S(11)$ at 4.181 μm, etc. Since most bipolar PNs show H_2 emissions (Kastner et al. 1996) due to shock excitation, contribution from H_2 lines is expected. In cases of evolved nebulae where there is no significant dust emission, rotational transitions of H_2 can in fact be the major contributor of the IRAC fluxes (Hora et al. 2006).

The key question is, therefore, "do our IRAC images reflect the distribution of the atomic, molecular, or solid-state components of PNs?" From the SEDs shown in Figure 16 we can see that in many cases the 5–8 μm region represents the beginning of the rise of the dust continuum emission that eventually peaks at $\sim$20–30 μm. So it is quite clear that at least in the long-wavelength bands (e.g., the 8 μm band) the image is dominated by dust emission, although this may include contribution from the features of the aromatic solid-state component. Molecular hydrogen is not expected to be a major factor, except in the 4.5 μm band, where there is no AIB emission.

Comparisons between the IRAC 8 μm images of bipolar PNs in our sample to the mid-infrared (10 and 20 μm) images of PNs observed with the Gemini Telescope show a lot of similarities (Volk et al. 2006). In addition to a bright central component (believed to originate from the torus), strong emissions are also seen in the lobes. Since there is no doubt that the Gemini images reflect dust emission, this conclusion can be reasonably extrapolated to the IRAC 8 μm images.

6. CONCLUSIONS

From the IRAC images of 30 PNs found in the GLIMPSE survey, we have found that most of the nebulae have extended dust emission. In cases where the nebulae show a bipolar morphology, dust is seen in the lobes in addition to the central regions. The 3–8 μm IRAC photometry also much better defines the SEDs of PNs, showing a clear distinction between the photospheric, nebular bound-free, and dust emission components. In some cases, the high fluxes in the 8.0 μm band suggest contribution from the 7.7 μm AIB emission, and the 8.0 μm band images therefore trace the distribution of aromatic materials in the nebulae. Since the discovery of PNs by optical means is likely to be incomplete due to galactic dust obscuration, the infrared properties of PNs in this sample provide a good guide for future discovery of galactic PNs through infrared surveys.

We thank the GLIMPSE team at the University of Wisconsin for their help in the processing of data. We also thank Kevin Volk for reducing the *ISO* spectra. This work is supported in part by the Natural Sciences and Engineering Council of Canada, the University of Hong Kong, and Academia Sinica, Taiwan. E. B. C. acknowledges support for this work from NASA contract 1224653 to the University of Wisconsin at Madison. This work is based on observations made with the *Spitzer Space Telescope*, which is operated by the Jet Propulsion Laboratory, California Institute of Technology, under a contract with NASA.

REFERENCES

Aaquist, O. B., & Kwok, S. 1990, A&A, 84, 229
Acker, A., Marcout, J., & Ochsenbein, F. 1996, First Supplement to the Strasbourg-ESO Catalogue of Galactic Planetary Nebulae (Strasbourg: Obs. Strasbourg)
Acker, A., et al. 1992, Strasbourg-ESO Catalogue of Galactic Planetary Nebulae (Strasbourg: Obs. Strasbourg)
Allen, L. E., et al. 2004, ApJS, 154, 363
Churchwell, E., et al. 2004, ApJ, 154, 332
———. 2006, ApJ, 649, 759
Cohen, M., et al. 2007, MNRAS, 374, 979
Condon, J. J., & Kaplan, D. L. 1998, ApJS, 117, 361
Corradi, R. L. M., & Schwarz, H. E. 1993, A&A, 278, 247
———. 1995, A&A, 293, 871
Fazio, G. G., et al. 2004, ApJS, 154, 10
Górny, S. K., Schwarz, H. E., Corradi, R. L. M., & Van Winckel, H. 1999, A&AS, 136, 145
Guerrero, M. A., Chu, Y.-H., & Gruendl, R. A. 2000, ApJ, 129, 295
Hora, J. L., Latter, W. B., Allen, L. E., Marengo, M., Deutsch, L. K., & Pipher, J. L. 2004, ApJS, 154, 296
Hora, J. L., Latter, W. B., Smith, H. A., & Marengo, M. 2006, ApJ, 652, 426
Hyung, S., Aller, L. H., & Feibelman, W. A. 1993, PASP, 105, 1279
Kastner, J. H., Weintraub, D. A., Gatley, I., Merrill, K. M., & Probst, R. G. 1996, ApJ, 462, 777
Kistiakowsky, V., & Helfand, D. J. 1995, AJ, 110, 2225
Kwok, S. 2000, The Origin and Evolution of Planetary Nebulae (Cambridge: Cambridge Univ. Press)
López-Martín, L., et al. 2002, A&A, 338, 652
MacLeod, G. C., et al. 1998, AJ, 116, 2936
Matsuura, M., Zijlstra, A. A., Gray, M. D., Molster, F. J., & Waters, L. B. F. M. 2005, MNRAS, 363, 628
Morgan, D. H., Parker, Q. A., & Cohen, M. 2003, MNRAS, 346, 719
Parker, Q. A., Phillipps, S., & Morgan, D. H. 1999, in ASP Conf. Ser. 168, New Perspectives on the Interstellar Medium, ed. A. R. Taylor, T. L. Landecker, & G. Joncas (San Francisco: ASP), 126
Parker, Q. A., et al. 2003a, in IAU Symp. 209, Planetary Nebulae: Their Evolution and Role in the Universe, ed. S. Kwok, M. A. Dopita, & R. Sutherland (San Francisco: ASP), 41
———. 2003b, in IAU Symp. 209, Planetary Nebulae: Their Evolution and Role in the Universe, ed. S. Kwok, M. A. Dopita, & R. Sutherland (San Francisco: ASP), 25
Parker, Q. A., et al. 2006, MNRAS, 373, 79
Parthasarathy, M., Acker, A., & Stenholm, B. 1998, A&A, 329, L9
Perinotto, M., Morbidelli, L., & Scatarzi, A. 2004, MNRAS, 349, 793
Pottasch, S. R., Beintema, D. A., & Feibelman, W. A. 2000, A&A, 363, 767
Schmeja, S., & Kimeswenger, S. 2002, Rev. Mex. AA, 12, 176
Vázquez, R., López-Martín, L., Miranda, L. F., Esteban, C., Torrelles, J. M., Arias, L., & Raga, A. C. 2000, A&A, 357, 1031
Whiteoak, J. B. Z. 1992, A&A, 262, 251
Wright, S. A., Corradi, R. L. M., & Perinotto, M. 2005, A&A, 436, 967
Volk, K., Hrivnak, B. J., & Kwok, S. 2006, in IAU Symp. 234, Planetary Nebulae in Our Galaxy and Beyond, ed. M. J. Barlow & R. H. Méndez (Cambridge: Cambridge Univ. Press), 535
Zhang, C. Y., & Kwok, S. 1991, A&A, 250, 179